guide cannula above the lateral ventricle (0.8 mm posterior and 1.5 mm lateral to bregma, 2.0 mm below the outer surface of the skull). The stereotaxic coordinates were guided by referring to the Atlas of Paxinos and Watson (Paxinos and Watson, 2005). The guide cannula was held firmly in place by dental acrylic cement. After surgery, the rats were individually returned to their cages and left to recover for 5 days or more until the following experiments.

von Frey filament test

Just before and 2 weeks after PSL, tactile sensitivity was measured using a calibrated von Frey filament ranging from 0.04 to 26 g (North Coast Medical, Morgan Hill, CA) as described previously (Ueda et al., 2010). Briefly, the animals were individually placed on an elevated wire mesh floor for testing. After a habituation period of 15–30 min, a tactile stimulus was applied to the middle plantar of the each paw by placing the von Frey filament perpendicular to the surface of the paw. The filament was held in this position with enough force to cause a slight bend. One trial involved 10 applications of filaments every 1–2 s. The threshold was determined to be the filament of the lowest stiffness, at which the rat responded (quick paw flick) in one or more of the trials. Rats that showed a lower threshold than preoperatively were considered to be demonstrating allodynia, and they were used in the following studies.

Effect of 5IA on tactile allodynia

For single administration, an injection cannula (o.d. 0.35 mm, i.d. 0.18 mm) was inserted 5.0 mm below the surface of the skull along the guide cannula. Various concentrations of 5IA (1, 3, 5, 10, 50, and 100 nmol dissolved in 5 μl of saline) or vehicle were then infused at 5 μl/rat with a constant rate of 10 μl/min using a microsyringe pump (EP-60, Eicom Corporation, Kyoto, Japan). Each group consisted of four to six animals. The injection cannula was retained in place for an additional 1 min to prevent a backflow of the drugs. Just before and 15, 30, 60, and 90 min after administration, tactile allodynia of the ligated paws were evaluated using the von Frey filament test. The results were expressed as a percentage of the maximal possible effect (%MPE) according to the following equation:

$$\%\mathrm{MPE} = \frac{\mathrm{Postdrugthreshold} - \mathrm{Predrugthreshold}}{\mathrm{Cut-off(26g)} - \mathrm{Predrugthreshold}} \times 100$$

For repetitive administration, the injection cannula was inserted, and an initial injection (5 or 50 nmol of 5IA dissolved in 5 μl of saline or vehicle) was performed using the method described earlier. A second injection of the same dose as that initially used was given 70 min later. Both groups consisted of four animals. Just before and 15, 30, 60, 85, 100, 130, and 160 min after the initial injection, tactile allodynia of the ligated paws was evaluated using the von Frey filament test, and %MPE values were calculated.

Autoradiographic study

For calculation of receptor occupancy, allodynia-expressing rats received an i.c.v. injection containing 370 kBq of [^{125}I]5IA with a vehicle or various concentrations of 5IA (1, 3, 5, 10, 50, and 100 nmol) concomitantly (n = 5–6 in each group). The injected volume was 5 μl. Fifteen or 90 min later, they were decapitated. Their brains were quickly removed, frozen in hexane (−80°C), and cut into 20 μm-thick coronal sections with a cryostat (JUNG CM3000, Leica Microsystems GmbH, Wetzlar, Germany). Autoradiograms were obtained, and quantitative analyses were performed according to a previously reported method (Kudo et al., 2009; Ueda et al., 2010). The data were expressed as a percentage of injected doses per gram of tissue (%ID/g) based on the data derived from ^{125}I autoradiographic microscale standards (Amersham Biosciences, Buckinghamshire, UK). Regions of interest were drawn over the thalamus, and the accumulated total radioactivity (%ID/g_T) was determined. Nonspecifically accumulated radioactivity (%ID/g_{NS}) was also determined using rats that were administered (−)-cytisine (1 mg/kg, 200 μl) intravenously for 5 min prior to i.c.v. injection of [^{125}I]5IA. The binding of [^{125}I]5IA was completely blocked by administering (−)-cytisine via this route in our previous study (Saji et al., 2002).

For the time course study of [^{125}I]5IA accumulation in the thalamus, normal rats received an i.c.v. injection containing 370 kBq/5 μl of [^{125}I]5IA (n = 5–6 in each group). Five, 15, 30, 60, and 90 min later, they were decapitated, and the following procedures were performed in a similar manner as described earlier.

Data analyses

Receptor occupancy was calculated as per previous reports (Liu et al., 2009; Miller et al., 2009) with a slight modification. The previous reports regarded binding of the probes in the reference region as nonspecific binding. However, in lacking an nAChR reference region, we used (−)-cytisine overloading to quantify the nonspecific binding of [^{125}I]5IA. The specific accumulation (%ID/g_S) of [^{125}I]5IA in the thalamus was obtained by subtracting the nonspecific accumulation from the corresponding total accumulation (%ID/g_T − %ID/g_{NS}). The specific accumulation to nonspecific accumulation ratio (SNR) was determined by dividing the specific accumulation by the nonspecific accumulation (%ID/g_S/%ID/g_{NS}). The receptor

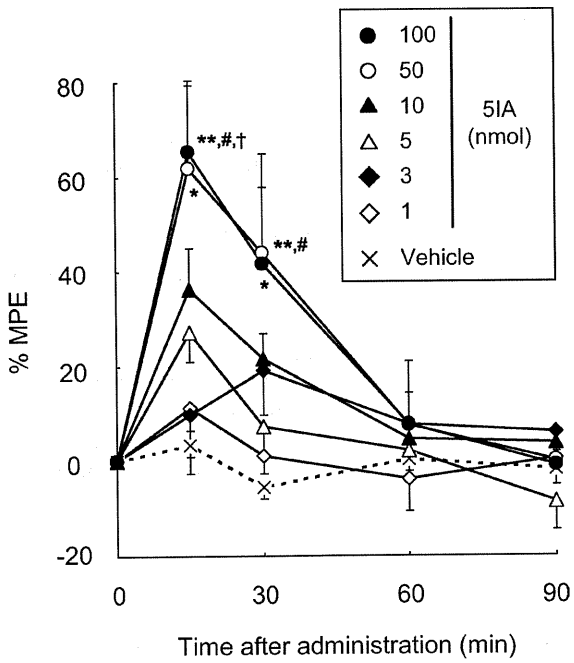

Fig. 1. Effects of multiple doses of 5IA on neuropathic tactile allodynia. 5IA was administered i.c.v. at time 0. Data are presented as a percentage of maximum possible effect (% MPE). Each point represents the mean ± SEM of ligated paws of four to six animals per group. $^{*}P < 0.05$, $^{**}P < 0.01$ vs. vehicle, $^{\#}P < 0.05$ vs. 1 nmol of 5IA, $^{\dagger}P < 0.05$ vs. 3 nmol of 5IA at same time point.

occupancy rate was then calculated according to following equation:

$$\%\text{Occupancy} = \frac{\text{SNR}_{\text{vehicle}} - \text{SNR}_{\text{5IA-loaded}}}{\text{SNR}_{\text{vehicle}}} \times 100$$

Statistical analyses

Analyses of the data from the von Frey filament test were performed using two-way analysis of variance (ANOVA) with repeated measures. If there was a significant difference, post-hoc one-way ANOVA followed by the Tukey–Kramer multiple comparison test was performed using each treatment combination as an independent group. Correlation coefficients were assessed with Spearman rank correlation coefficients. Differences were considered significant at $P < 0.05$.

RESULTS

Antiallodynic effect of single administration of 5IA

Paw withdrawal thresholds decreased from 12.2 ± 1.3 g to 3.4 ± 0.4 g in ligated paws. Effects of i.c.v. administeration of 5IA on paw withdrawal thresholds are shown in Figure 1. Two-way ANOVA demonstrated significant main effects of treatment ($F_{6,\ 118} = 4.55$, $P = 0.002$) and time ($F_{3,\ 118} = 24.2$, $P < 0.001$), and a significant interaction between treatment and time ($F_{18,\ 118} = 3.10$, $P < 0.001$). A significant and dose-dependent antiallodynic effect was observed 15 and 30 min after administration (vehicle: 3 ± 6, 50 nmol: 62 ± 17, 100 nmol: 65 ± 15 at 15 min). On the other hand, the effects were disappeared 90 min after administration (vehicle: −2 ± 3, 100 nmol: −1 ± 3) (Fig. 1).

TABLE I. Thalamic nAChR occupancy by 5IA after i.c.v. administration

Dose (nmol)	%RO at 15 min	%RO at 90 min
1	14 ± 7.1	n.d.
3	22 ± 8.8	n.d.
5	41 ± 21	55 ± 1.4
10	63 ± 10	n.d.
50	79 ± 7.0	94 ± 1.3
100	81 ± 6.9	99 ± 0.5

Data represent the mean ± SEM for five to six animals per group.%RO: % receptor occupancy; n.d.: not determined.

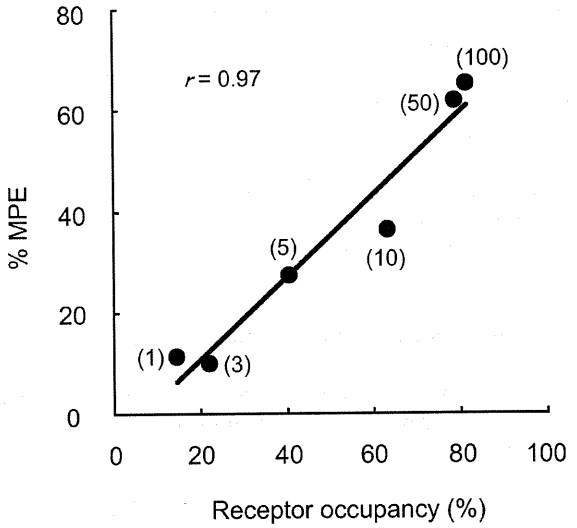

Fig. 2. Correlation between antiallodynic effect and receptor occupancy at 15 min after i.c.v. administration of 5IA. The ordinate indicates the antiallodynic effect of multiple doses of 5IA and the abscissa indicates thalamic nAChR occupancy by the same doses of 5IA. The number in parentheses is the amount of 5IA administered. Each point represents the mean for four to six animals per group. The correlation coefficient (r) is 0.97, indicating a significant high correlation ($P < 0.05$). MPE, maximal possible effect.

Relationship between thalamic nAChR occupancy by 5IA and antiallodynic effect

The time course study revealed that the specific accumulation of [^{125}I]5IA in the thalamus increased in a time-dependent manner, and reached a plateau (1.5% ± 0.3% ID/g) at 30 min after administration (data not shown). Next, thalamic nAChR occupancy by 5IA was determined 15 and 90 min after i.c.v. administration. The results are shown in Table I. Both nAChR occupancy rates and antiallodynic effect reached a plateau at 50 or 100 nmol of 5IA. Figure 2

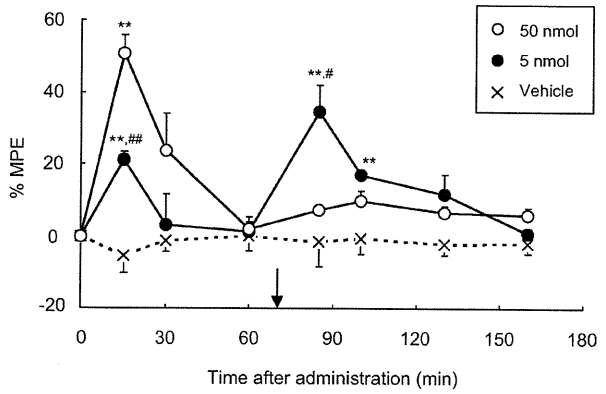

Fig. 3. Antiallodynic effect of 5IA on neuropathic tactile allodynia after repetitive i.c.v. administration. The arrow indicates the time point of second administration (70 min after first administration). Data are presented as a percentage of maximum possible effect (% MPE). Each point represents the mean ± SEM of the ligated paws of four animals per group. $^{*}P < 0.05$, $^{**}P < 0.01$ vs. vehicle, $^{\#}P < 0.05$, $^{\#\#}P < 0.01$ vs. 50 nmol of 5IA at the same time point.

shows a relationship between nAChR occupancy and antiallodynic effect at 15 min after i.c.v. administration, revealing a high positive correlation between them ($r = 0.97$, $P < 0.05$). On the other hand, receptor occupancy rates did not decrease at 90 min after administration, although the antiallodynic effects were disappeared.

Antiallodynic effect of repetitive administered 5IA

We administered 5IA at 0 and 70 min, and performed the von Frey filament test. The result is shown in Fig. 3. Two-way ANOVA demonstrated significant main effects of treatment ($F_{2, 63} = 14.5$, $P = 0.002$) and time ($F_{6, 63} = 7.48$, $P < 0.001$), and a significant interaction between treatment and time ($F_{12, 63} = 6.73$, $P < 0.001$). When administered 5 nmol of 5IA, which occupied about 40% of nAChRs in the thalamus, a significant antiallodynic effect was observed at 15 min (vehicle: -5 ± 5, 5 nmol: 21 ± 2). The effect diminished completely at 60 min (vehicle: 0.1 ± 4, 5 nmol: 1 ± 4). Fifteen minutes after the second administration at 70 min, a significant antiallodynic effect was observed again (vehicle: -1 ± 7, 5 nmol: 35 ± 7).

When 50 nmol of 5IA was administered, which occupied approximately 80% of nAChRs in the thalamus, a significant antiallodynic effect was also found at 15 min (50 nmol: 51 ± 5), and the effect decreased at 60 min (50 nmol: 2 ± 2). In contrast to the significant antiallodynic effects observed after both the initial and second administration of 5 nmol of 5IA, repetitive administration of 50 nmol of 5IA did not produce an antiallodynic effect at 85 min (15 min after the second administration) (50 nmol: 7 ± 1).

DISCUSSION

Numerous studies have shown the antinociceptive effects of nicotine in a variety of preclinical pain models (Iwamoto and Marion, 1993; Jain, 2004; Kiguchi et al., 2008). However, antinociception in animals has been typically found to be of limited duration and attenuated with repeated dosing (Decker et al., 2004). Epibatidine also has been found to have a relatively short duration of action, with a substantial decay in effects observed within the first 30 min after administration, although it is a very potent antinociceptive agent with broad-spectrum activity (Gilbert et al., 2001). Antinociceptive effects of other nAChR agonists (A-85380 and ABT-594) have also been found to diminish until 120 min after administration (Bannon et al., 1998; Rueter et al., 2003). Thus, the relatively short duration of action has been suggested as a common problem of nAChR agonists.

In this study, we demonstrated a dose-dependent antiallodynic effect of 5IA 15 min after i.c.v. administration. The effect disappeared 60 min or 90 min after administration. These results are consistent with our previous report (Ueda et al., 2010). Since the maximum antiallodynic effect was observed 15 min after administration, we measured receptor occupancy rates at the same time point and compared them with each other. In result, a high positive correlation was observed between them in the thalamus (Fig. 2). This result is consistent with our previous finding that the nAChRs expressed in the thalamus mediated the antiallodynic effect (Ueda et al., 2010).

We then attempted to explore the reason why the antiallodynic effect of 5IA disappeared at 90 min after administration. The examination of temporal changes in thalamic [^{125}I]5IA accumulation revealed that, rather than decreasing, [^{125}I]5IA accumulation increased in a time-dependent manner, reaching a plateau at 30 min. Furthermore, the receptor occupancy rates at 90 min tended to be greater than those at 15 min (Table I). A time-dependent clearance from the thalamus of 5IA not bound to nAChRs may be responsible for the increase in receptor occupancy rates. These results demonstrated that 5IA continues binding to nAChRs in the thalamus for at least 90 min after i.c.v. administration. Thus, the disappearance of antiallodynic effects was not due to the clearance of 5IA from the thalamus.

It is well known that nAChRs can undergo desensitization, a reversible reduction in response during sustained agonist application. Buisson et al. found that recovery from epibatidine-induced desensitization is very slow using a cell line stably expressed nAChRs. The authors suggested that epibatidine may have remained tightly bound to nAChRs in a nonactivatable state because of its extremely high affinity (Buisson et al., 2000). In an in-vivo experiment, the repetitive administration of epibatidine

intrathecally within 30 min actually resulted a significant reduction of apparent antinociceptive effects (Khan et al., 1998). Thus, epibatidine may induce desensitization of nAChRs by binding to them persistently in vivo.

For this reason, we examined the possibility of desensitization of nAChRs caused by the persistent binding of 5IA. The similarity between 5IA and [^{125}I]5IA is an appropriate property to use for deciding on the two doses of 5IA: one is the dose used to produce a significant antiallodynic effect with full receptor occupancy; and the other is the dose used to produce a significant antiallodynic effect with leaving unoccupied nAChRs. Based on the results shown in Figure 2, we decided on the following two dosages: a dose of 5 nmol, which had shown half-maximal occupancy rates; and a dose of 50 nmol, which had shown the maximal occupancy rates. When administered 5 nmol of 5IA, approximately 50% of nAChRs in the thalamus were occupied 90 min after the initial administration. Therefore, 50% of the nAChRs in the thalamus probably existed still free at the second administration. With these unoccupied nAChRs, 5IA could bind them and produce an antiallodynic effect again after the second administration. Conversely, 50 nmol of 5IA already occupied 80% of the nAChRs, with almost all the receptors kept occupying and temporarily inactive at the second administration. There were probably few available nAChRs in the thalamus; and thus, the second 5IA administration could not produce a significant effect.

Many studies have shown that α4-subunit-containing nAChRs, probably α4β2 nAChRs, play an important role in nAChR-mediated antinociception (Bitner et al., 1998, 2000; Marubio et al., 1999). Since it has been reported that α4β2 nAChRs desensitize slowly (in terms of seconds) but are very prone to desensitization (Giniatullin et al., 2005), the relatively short duration of the antiallodynic effect produced by nAChR agonists was accounted for by the desensitization of α4β2 nAChRs. This suggests that there may be therapeutic benefits of positive allosteric modulators (PAMs) of α4β2 nAChRs, although the therapeutic potential of α4β2 nAChRs has been amply documented through use of selective agonists (Decker et al., 2004; Jain, 2004; Rowbotham et al., 2009). PAMs would not be expected to induce cumulative receptor desensitization and should act in a manner consistent with the timing and localization of endogenous cholinergic neurotransmission. For such reasons, the research efforts of pharmaceutical companies are now also focused on PAMs (Changeux, 2010; Taly et al., 2009).

The involvement of α7 nAChRs in antinociceptive effects is controversial. Some studies have found α7-nAChR ligands to be efficacious (Young et al., 2008) while others have not (Gao et al., 2010). Muhkin et al. reported that the α7/α4β2 affinity ratio of 5IA, calculated from the Ki value, was 25,000, indicating a high selectivity of 5IA for α4β2 nAChRs (Mukhin et al., 2000). Perry et al. (2002) have reported that nAChRs expressed in the thalamus are mainly of the α4β2 subtype, and thus the antiallodynic effect observed when 5IA bound to thalamic nAChRs was probably mediated via α4β2 nAChRs. However, 5IA might act on α7 and/or other nAChRs expressed in extrathalamic (central) or peripheral regions after the systemic administration of large doses in vivo. Relationships between receptor occupancy rates in these regions and antiallodynic effects remain uncertain.

In summary, we measured the thalamic nAChR occupancy rates by 5IA in the PSL model of neuropathic pain, and then compared them to antiallodynic effects. A significant and dose-dependent antiallodynic effect was observed 15 min after i.c.v. administration of 5IA. It was highly correlated with receptor occupancy rates, consistent with our previous finding that nAChRs expressed in the thalamus mediate the antiallodynic effect. On the other hand, the antiallodynic effect was diminished in a short time, although thalamic nAChRs were kept occupying by 5IA 90 min after administration. A low dose of 5IA (which showed low receptor occupancy rates) exhibited a significant antiallodynic effect after the second administration, while a high dose of 5IA (which occupied almost all the thalamic nAChRs) showed no effect. These findings suggest that not clearance of 5IA but desensitization of nAChRs caused by persistent binding of 5IA is responsible for the disappearance of the antiallodynic effect.

REFERENCES

Bannon AW, Decker MW, Kim DJ, Campbell JE, Arneric SP. 1998. ABT-594, a novel cholinergic channel modulator, is efficacious in nerve ligation and diabetic neuropathy models of neuropathic pain. Brain Res 801:158–163.

Bitner RS, Nikkel AL, Curzon P, Arneric SP, Bannon AW, Decker MW. 1998. Role of the nucleus raphe magnus in antinociception produced by ABT-594: Immediate early gene responses possibly linked to neuronal nicotinic acetylcholine receptors on serotonergic neurons. J Neurosci 18:5426–5432.

Bitner RS, Nikkel AL, Curzon P, Donnelly-Roberts DL, Puttfarcken PS, Namovic M, Jacobs IC, Meyer MD, Decker MW. 2000. Reduced nicotinic receptor-mediated antinociception following in vivo antisense knock-down in rat. Brain Res 871:66–74.

Brasic JR, Zhou Y, Musachio JL, Hilton J, Fan H, Crabb A, Endres CJ, Reinhardt MJ, Dogan AS, Alexander M, Rousset O, Maris MA, Galecki J, Nandi A, Wong DF. 2009. Single photon emission computed tomography experience with (*S*)-5-[^{123}I]iodo-3-(2-azetidinylmethoxy)pyridine in the living human brain of smokers and nonsmokers. Synapse 63:339–358.

Buisson B, Vallejo YF, Green WN, Bertrand D. 2000. The unusual nature of epibatidine responses at the alpha4beta2 nicotinic acetylcholine receptor. Neuropharmacology 39:2561–2569.

Changeux JP. 2010. Allosteric receptors: From electric organ to cognition. Annu Rev Pharmacol Toxicol 50:1–38.

Court JA, Martin-Ruiz C, Graham A, Perry E. 2000. Nicotinic receptors in human brain: Topography and pathology. J Chem Neuroanat 20:281–298.

Decker MW, Rueter LE, Bitner RS. 2004. Nicotinic acetylcholine receptor agonists: A potential new class of analgesics. Curr Top Med Chem 4:369–384.

Dwoskin LP, Smith AM, Wooters TE, Zhang Z, Crooks PA, Bardo MT. 2009. Nicotinic receptor-based therapeutics and candidates for smoking cessation. Biochem Pharmacol 78:732–743.

Flores CM, Rogers SW, Pabreza LA, Wolfe BB, Kellar KJ. 1992. A subtype of nicotinic cholinergic receptor in rat brain is composed of alpha 4 and beta 2 subunits and is up-regulated by chronic nicotine treatment. Mol Pharmacol 41:31–37.

Fujita M, Ichise M, Van Dyck CH, Zoghbi SS, Tamagnan G, Mukhin AG, Bozkurt A, Seneca N, Tipre D, DeNucci CC, Iida H, Vaupel DB, Horti AG, Koren AO, Kimes AS, London ED, Seibyl JP, Baldwin RM, Innis RB. 2003. Quantification of nicotinic acetylcholine receptors in human brain using [^{123}I]5-I-A-85380 SPET. Eur J Nucl Med Mol Imaging 30:1620–1629.

Gao B, Hierl M, Clarkin K, Juan T, Nguyen H, Valk M, Deng H, Guo W, Lehto SG, Matson D, McDermott JS, Knop J, Gaida K, Cao L, Waldon D, Albrecht BK, Boezio AA, Copeland KW, Harmange JC, Springer SK, Malmberg AB, McDonough SI. 2010. Pharmacological effects of nonselective and subtype-selective nicotinic acetylcholine receptor agonists in animal models of persistent pain. Pain 149:33–49.

Gilbert SD, Clark TM, Flores CM. 2001. Antihyperalgesic activity of epibatidine in the formalin model of facial pain. Pain 89:159–165.

Giniatullin R, Nistri A, Yakel JL. 2005. Desensitization of nicotinic ACh receptors: Shaping cholinergic signaling. Trends Neurosci 28: 371–378.

Iwamoto ET, Marion L. 1993. Adrenergic, serotonergic and cholinergic components of nicotinic antinociception in rats. J Pharmacol Exp Ther 265:777–789.

Jain KK. 2004. Modulators of nicotinic acetylcholine receptors as analgesics. Curr Opin Investig Drugs 5:76–81.

Khan IM, Buerkle H, Taylor P, Yaksh TL. 1998. Nociceptive and antinociceptive responses to intrathecally administered nicotinic agonists. Neuropharmacology 37:1515–1525.

Kiguchi N, Maeda T, Tsuruga M, Yamamoto A, Yamamoto C, Ozaki M, Kishioka S. 2008. Involvement of spinal Met-enkephalin in nicotine-induced antinociception in mice. Brain Res 1189: 70–77.

Kudo T, Ueda M, Kuge Y, Mukai T, Tanaka S, Masutani M, Kiyono Y, Kizaka-Kondoh S, Hiraoka M, Saji H. 2009. Imaging of HIF-1-active tumor hypoxia using a protein effectively delivered to and specifically stabilized in HIF-1-active tumor cells. J Nucl Med 50: 942–949.

Lindstrom J, Anand R, Peng X, Gerzanich V, Wang F, Li Y. 1995. Neuronal nicotinic receptor subtypes. Ann N Y Acad Sci 757:100–116.

Liu X, Vilenski O, Kwan J, Apparsundaram S, Weikert R. 2009. Unbound brain concentration determines receptor occupancy: A correlation of drug concentration and brain serotonin and dopamine reuptake transporter occupancy for eighteen compounds in rats. Drug Metab Dispos 37:1548–1556.

Mamede M, Ishizu K, Ueda M, Mukai T, Iida Y, Fukuyama H, Saga T, Saji H. 2004. Quantification of human nicotinic acetylcholine receptors with ^{123}I-5IA SPECT. J Nucl Med 45:1458–1470.

Mamede M, Ishizu K, Ueda M, Mukai T, Iida Y, Kawashima H, Fukuyama H, Togashi K, Saji H. 2007. Temporal change in human nicotinic acetylcholine receptor after smoking cessation: 5IA SPECT study. J Nucl Med 48:1829–1835.

Marubio LM, del Mar Arroyo-Jimenez M, Cordero-Erausquin M, Lena C, Le Novere N, de Kerchove d'Exaerde A, Huchet M, Damaj MI, Changeux JP. 1999. Reduced antinociception in mice lacking neuronal nicotinic receptor subunits. Nature 398:805–810.

Miller TR, Milicic I, Bauch J, Du J, Surber B, Browman KE, Marsh K, Cowart M, Brioni JD, Esbenshade TA. 2009. Use of the H_3 receptor antagonist radioligand [^{3}H]-A-349821 to reveal in vivo receptor occupancy of cognition enhancing H3 receptor antagonists. Br J Pharmacol 157:139–149.

Mitsis EM, Cosgrove KP, Staley JK, Bois F, Frohlich EB, Tamagnan GD, Estok KM, Seibyl JP, van Dyck CH. 2009a. Age-related decline in nicotinic receptor availability with [^{123}I]5-IA-85380 SPECT. Neurobiol Aging 30:1490–1497.

Mitsis EM, Reech KM, Bois F, Tamagnan GD, Macavoy MG, Seibyl JP, Staley JK, van Dyck CH. 2009b. ^{123}I-5-IA-85380 SPECT imaging of nicotinic receptors in Alzheimer disease and mild cognitive impairment. J Nucl Med 50:1455–1463.

Mukhin AG, Gundisch D, Horti AG, Koren AO, Tamagnan G, Kimes AS, Chambers J, Vaupel DB, King SL, Picciotto MR, Innis RB, London ED. 2000. 5-Iodo-A-85380, an alpha4beta2 subtype-selective ligand for nicotinic acetylcholine receptors. Mol Pharmacol 57:642–669.

Mukhin AG, Kimes AS, Chefer SI, Matochik JA, Contoreggi CS, Horti AG, Vaupel DB, Pavlova O, Stein EA. 2008. Greater nicotinic acetylcholine receptor density in smokers than in nonsmokers: A PET study with 2-^{18}F-FA-85380. J Nucl Med 49:1628–1635.

Ogawa M, Tsukada H, Hatano K, Ouchi Y, Saji H, Magata Y. 2009. Central in vivo nicotinic acetylcholine receptor imaging agents for positron emission tomography (PET) and single photon emission computed tomography (SPECT). Biol Pharm Bull 32:337–340.

Oishi N, Hashikawa K, Yoshida H, Ishizu K, Ueda M, Kawashima H, Saji H, Fukuyama H. 2007. Quantification of nicotinic acetylcholine receptors in Parkinson's disease with ^{123}I-5IA SPECT. J Neurol Sci 256:52–60.

Paterson D, Nordberg A. 2000. Neuronal nicotinic receptors in the human brain. Prog Neurobiol 61:75–111.

Paxinos G, Watson C. 2005. The rat brain in stereotaxic coordinates, 5th ed. San Diego: Elsevier Academic Press.

Perry DC, Xiao Y, Nguyen HN, Musachio JL, Davila-Garcia MI, Kellar KJ. 2002. Measuring nicotinic receptors with characteristics of alpha4beta2, alpha3beta2 and alpha3beta4 subtypes in rat tissues by autoradiography. J Neurochem 82:468–481.

Rowbotham MC, Duan WR, Thomas J, Nothaft W, Backonja MM. 2009. A randomized, double-blind, placebo-controlled trial evaluating the efficacy and safety of ABT-594 in patients with diabetic peripheral neuropathic pain. Pain 146:245–252.

Rueter LE, Kohlhaas KL, Curzon P, Surowy CS, Meyer MD. 2003. Peripheral and central sites of action for A-85380 in the spinal nerve ligation model of neuropathic pain. Pain 103:269–276.

Saji H, Ogawa M, Ueda M, Iida Y, Magata Y, Tominaga A, Kawashima H, Kitamura Y, Nakagawa M, Kiyono Y, Mukai T. 2002. Evaluation of radioiodinated 5-iodo-3-(2(*S*)-azetidinylmethoxy)pyridine as a ligand for SPECT investigations of brain nicotinic acetylcholine receptors. Ann Nucl Med 16:189–200.

Seltzer Z, Dubner R, Shir Y. 1990. A novel behavioral model of neuropathic pain disorders produced in rats by partial sciatic nerve injury. Pain 43:205–218.

Staley JK, van Dyck CH, Weinzimmer D, Brenner E, Baldwin RM, Tamagnan GD, Riccardi P, Mitsis E, Seibyl JP. 2005. ^{123}I-5-IA-85380 SPECT measurement of nicotinic acetylcholine receptors in human brain by the constant infusion paradigm: Feasibility and reproducibility. J Nucl Med 46:1466–1472.

Taly A, Corringer PJ, Guedin D, Lestage P, Changeux JP. 2009. Nicotinic receptors: Allosteric transitions and therapeutic targets in the nervous system. Nat Rev Drug Discov 8:733–750.

Ueda M, Iida Y, Mukai T, Mamede M, Ishizu K, Ogawa M, Magata Y, Konishi J, Saji H. 2004. 5-[^{123}I]Iodo-A-85380: Assessment of pharmacological safety, radiation dosimetry and SPECT imaging of brain nicotinic receptors in healthy human subjects. Ann Nucl Med 18:337–344.

Ueda M, Iida Y, Kitamura Y, Kawashima H, Ogawa M, Magata Y, Saji H. 2008. 5-Iodo-A-85380, a specific ligand for alpha4beta2 nicotinic acetylcholine receptors, prevents glutamate neurotoxicity in rat cortical cultured neurons. Brain Res 1199:46–52.

Ueda M, Iida Y, Tominaga A, Yoneyama T, Ogawa M, Magata Y, Nishimura H, Kuge Y, Saji H. 2010. Nicotinic acetylcholine receptors expressed in the ventral posterolateral thalamic nucleus play an important role in anti-allodynic effects. Br J Pharmacol 159: 1201–1210.

Young T, Wittenauer S, Parker R, Vincler M. 2008. Peripheral nerve injury alters spinal nicotinic acetylcholine receptor pharmacology. Eur J Pharmacol 590:163–169.

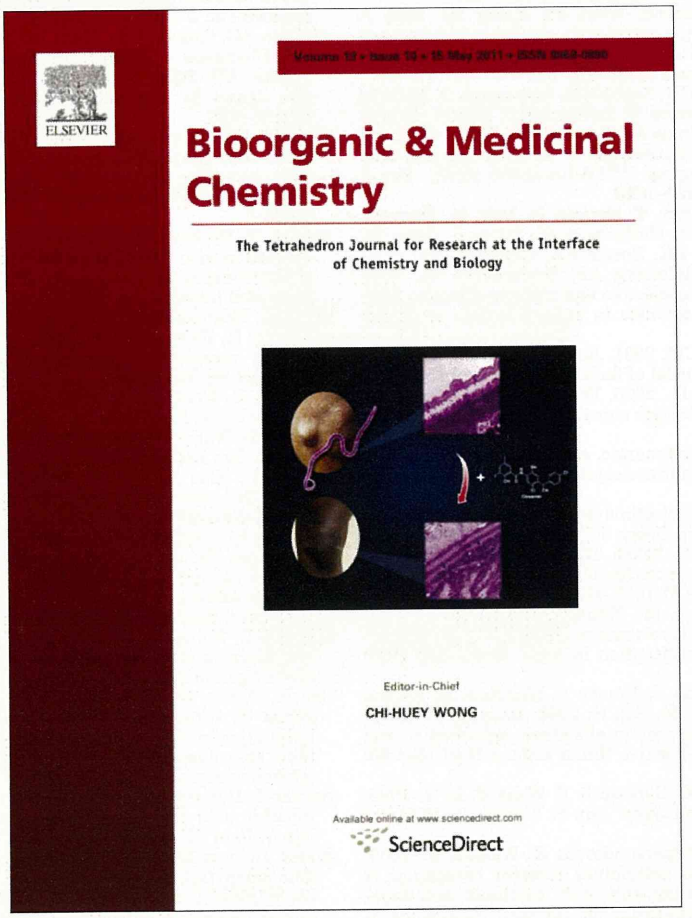

Bioorganic & Medicinal Chemistry 19 (2011) 3216–3220

Contents lists available at ScienceDirect

Bioorganic & Medicinal Chemistry

journal homepage: www.elsevier.com/locate/bmc

Concise site-specific synthesis of DTPA–peptide conjugates: Application to imaging probes for the chemokine receptor CXCR4

Ryo Masuda, Shinya Oishi *, Hiroaki Ohno, Hiroyuki Kimura, Hideo Saji, Nobutaka Fujii *

Graduate School of Pharmaceutical Sciences, Kyoto University, Sakyo-ku, Kyoto 606-8501, Japan

ARTICLE INFO

Article history:
Received 17 February 2011
Revised 25 March 2011
Accepted 26 March 2011
Available online 2 April 2011

Keywords:
CXCR4
DTPA
Molecular imaging

ABSTRACT

Diethylenetriaminepentaacetic acid (DTPA) is a useful chelating agent for radionuclides such as ^{68}Ga, ^{99m}Tc and ^{111}In, which are applicable to nuclear medicine imaging. In this study, we established a facile synthetic protocol for the production of mono-DTPA-conjugated peptide probes. A novel monoreactive DTPA precursor reagent was synthesized in two steps using the chemistry of the *o*-nitrobenzenesulfonyl (Ns) protecting group, and under mild conditions this DTPA precursor was incorporated onto an N^{ε}-bromoacetylated Lys of a protected peptide resin. The site-specific DTPA conjugation was facilitated by using a highly acid-labile 4-methyltrityl (Mtt) protecting group for the target site of the bioactive peptide during the solid-phase synthesis. A combination of both techniques yielded peptides with disulfide bonds, such as octreotide and polyphemusin II-derived CXCR4 antagonists. DTPA–peptide conjugates were purified in a single step following cleavage from the resin and disulfide bond formation. This site-specific on-resin construction strategy was used for the design and synthesis of a novel In-DTPA-labeled CXCR4 antagonist, which exhibited highly potent inhibitory activity against SDF-1–CXCR4 binding.

1. Introduction

Recent progress in molecular imaging methodologies such as positron emission tomography (PET), single-photon emission computed tomography (SPECT) and optical imaging technologies has significantly improved the early detection and diagnosis of malignant tumors. To visualize the specific molecular events involved in the physiological and/or pathological processes, a number of peptide-based imaging probes have been developed for overexpressed receptors of peptide hormones and extracellular matrix proteins.[1] These probes are usually designed by a combination of three components: a target-specific vector peptide, an imaging part such as a radionuclide or fluorophore, and a linker to covalently or noncovalently conjugate the peptide with the imaging moiety. The addition of a functional moiety onto small-sized bioactive peptides may be highly susceptible to interaction with receptors or counterpart molecules. Consequently, there have been many reagents of choice for appropriate protein/peptide modifications. In addition, to determine the best labeling position from structure-function relationship studies, versatile synthetic approaches toward various types of labeled peptide are desired.

Polyamino polycarboxylate ligands efficiently coordinate metal radioisotopes to aid the radiolabeling of bioactive peptides. Among the chelating ligands, 1,4,7,10-tetraazacyclododecane-1,4,7,10-tetraacetic acid (DOTA) **1a** has been most widely utilized, since a variety of metal radioisotopes for both diagnostic and therapeutic purposes form complexes with high affinity and kinetic stability (Fig. 1).[2] DOTA-modification of bioactive peptides is facilitated by commercially available reagents such as DOTA-NHS **1b** and DOTA-maleimide **1c** to provide the expected peptides in a single step.[3,4] Alternatively, tris(*tert*-butyl)-DOTA **2a** with a free carboxyl group is employed for the modification of an amino group of protected peptides bound to solid-supports.[5] Lysine or phenylalanine derivatives **2b,c** possessing a *tert*-butyl-protected DOTA moiety are also useful components for the peptide sequence assembly.[6] *tert*-Butyl protecting groups in these reagents are easily removed during the final side-chain deprotection process of peptide synthesis.

In contrast to these DOTA derivatives, there has been limited work exploring the application of the diethylenetriaminepentaacetic acid (DTPA) chelating group **3a**, although DTPA represents a promising alternative, especially for ^{68}Ga, ^{99m}Tc and ^{111}In (Fig. 1). The recent success of DTPA-based probes is exemplified by a glucagon-like peptide-1 (GLP-1) receptor ligand, [Lys^{40}(Ahx-DTPA-^{111}In)NH_2]-exendin-4, for insulinoma diagnosis.[7] The DTPA group also works as a more favorable functional group than DOTA to facilitate the biological or biodistribution properties of several probes.[8] For the preparation of DTPA-conjugated imaging probes, several conjugation reagents have been developed. The most familiar cyclic diethylenetriaminepentaacetic dianhydride **4**

* Corresponding authors. Tel.: +81 75 753 4551; fax: +81 75 753 4570.
E-mail addresses: soishi@pharm.kyoto-u.ac.jp (S. Oishi), nfujii@pharm.kyoto-u.ac.jp (N. Fujii).

0968-0896/$ - see front matter © 2011 Elsevier Ltd. All rights reserved.
doi:10.1016/j.bmc.2011.03.059

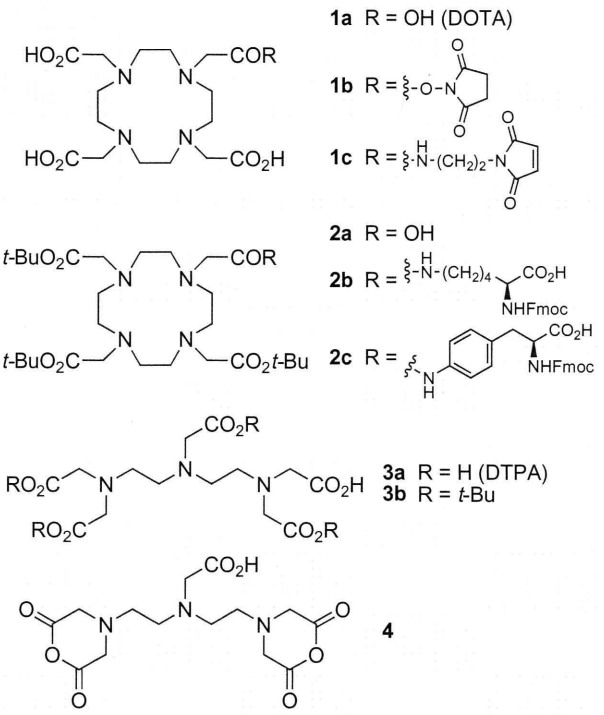

Figure 1. Structures of radionuclide chelating agents and the precursors.

is a bifunctional chelating agent, which can conjugate with peptide hormones and antibodies.[9] Using this reagent, concomitant formations of a bis-conjugated product[10] and intra- and intermolecular cross-linked products[11] were unavoidable. Monoreactive DTPA derivatives have also been developed for the preparation of DTPA–peptide conjugates without the unfavorable by-product formations.[12,13] For example, we reported the synthesis and application of 3,6,9,9-tetrakis[(*tert*-butoxycarbonyl)methyl]-3,6,9-triazanonanoic acid **3b** (mDTPA),[14] in which the four carboxylates were protected with *tert*-butyl ester. However, a longer process from the commercially available reagents is required for the synthesis of these DTPA-conjugation reagents (Scheme 1A).

Accordingly, to establish a facile and efficient synthetic method for DTPA–peptide conjugates, we have investigated the site-specific and on-resin construction of a DTPA moiety. Herein, we describe the short-step synthesis of a DTPA precursor using the *o*-nitrobenzenesulfonyl (Ns) protecting group and the solid-phase synthesis of DTPA–peptide conjugates. The design and synthesis of DTPA–peptide conjugates that potentially target the somatostatin receptor and chemokine receptor CXCR4 are also presented.[15]

2. Results and discussion

2.1. Synthesis of a DTPA-conjugation reagent and the application to octreotide derivatives

The synthetic scheme for the production of mDTPA reagent **10**, as described in our previous study, is presented in Scheme 1A. We hypothesized that two remedies could significantly improve the overall synthetic process of DTPA–peptide conjugates. First, the use of an Ns group in place of the trifluoroacetyl group was expected to serve as a temporary protecting group and an auxiliary group for global modification with four *tert*-butoxycarbonylmethyl groups. This potentially improves the stepwise synthesis of the intermediate **7** in the solution-phase. In addition, a secondary amine **8** as a nucleophilic precursor for the bromoacetyl group on peptide resin **11** can directly produce the overall DTPA framework of **12** on the solid support without the additional three-step modification process of **8** in solution (Scheme 1B).[16]

Synthesis of DTPA precursor **8** began with mono-Ns protection of the commercially available diethylenetriamine **5** (Scheme 2). The Ns-protected intermediate was successively treated with excess equivalent of *t*-butyl bromoacetate in a one-pot process. Although the solvent EtOH has been reported to be effective in predominantly giving the mono-Ns product,[17] concomitant production of bis-Ns product **14b** was not suppressed as in DMF. The treatment of excess diethylenetriamine **5** with NsCl in EtOH provided mono-Ns product **14a** in 65% yield (calculated based on NsCl), which can be readily purified by chromatography. Compound **14a** was then subjected to deprotection with mercaptoacetic acid and LiOH to provide the expected precursor **8** in 77% yield.

Using the resulting reagent **8**, DTPA-conjugation of [D-Phe^1]octreotide was investigated as a model study (Scheme 3), which is employed as a radionuclide imaging probe for the somatostatin receptor.[14,18,19] After peptide-chain elongation by Fmoc-based solid-phase peptide synthesis, the N-terminus of **16** was modified with bromoacetic acid and 1,3-diisopropylcarbodiimide (DIC). Subsequently, the bromide **17** was treated with the reagent **8** in the presence of $(i\text{-Pr})_2$NEt to provide the fully protected peptide resin **18a**. Cleavage from the resin **18a** and disulfide formation under air-oxidation conditions provided [DTPA-D-Phe^1]octreotide **19a** with high purity. The bromoacetylated peptide **17** was also modified with commercially available DOTA precursor reagent **20**, using the identical procedure to provide [DOTA-D-Phe^1]octreotide **19b**.[20] These suggest that this on-resin modification procedure is widely applicable to any chelating reagents with nucleophilic functional groups such as DTPA and DOTA precursors.

2.2. Site-specific DTPA-conjugation of bioactive peptides: synthesis of CXCR4 receptor probes

It has been reported that a high level of CXCR4 expression in tumors is associated with malignant and metastatic properties.[21] Intrinsic SDF-1 release from the potential distal metastatic sites mediates organ-specific metastasis of CXCR4-expressing cells from the primary lesions. Since CXCR4-expressing cancer stem cells are related to the metastatic spread in orthotopic primary tumors,[22] it is of considerable importance to develop potent CXCR4-imaging probes to detect potential cancer stem cells within malignant tumors, as exemplified by the diagnosis of bladder cancer by a fluorescent CXCR4 probe.[23,24]

Previously, we reported a DTPA-conjugated CXCR4 antagonist, DTPA-Ac-TZ14011 **26a**,[25] which was designed from a horseshoe crab-derived anti-HIV peptide T140. This peptide has β-sheet-like structures maintained by a disulfide bond, around which the pharmacophore residues for bioactivity are located.[26] For the site-specific conjugation at D-Lys^8 in the type II' β-turn region of T140 with a single DTPA group in the solution-phase, a secondary lysine (Lys^7) was substituted with arginine, which cannot be acylated by standard reagents.[25] Although a DTPA group was successfully ligated with maintenance of highly potent CXCR4 antagonistic activity in this case,[25] the accompanying substitutions needed for specific modification of other peptides may possibly lead to a decrease in the bioactivity. Therefore, we planned the facile site-specific DTPA conjugation on a solid-support for production of CXCR4 imaging probes without substitution of the secondary Lys^7 residue. To distinguish D-Lys^8 to be labeled in peptides **26**, the highly acid-labile 4-methyltrityl (Mtt) group was exploited for temporary protection of the ε-amino group during solid-phase peptide synthesis.[27] For the other Lys residues such as Lys^7 of

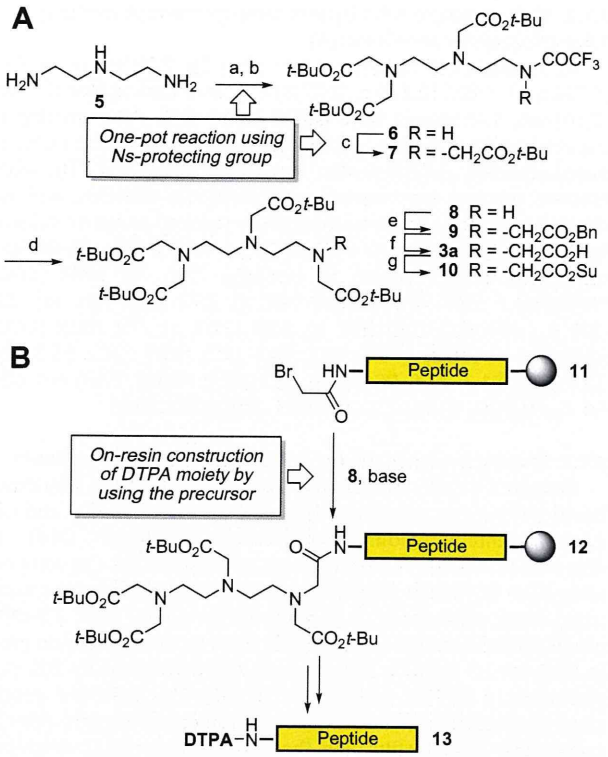

Scheme 1. (A) Synthetic scheme for the DTPA-conjugation reagent **10** prepared in our previous study; (B) synthetic plan for the DTPA-conjugated peptides in this study. Reagents: (a) CF_3CO_2Et; (b) $BrCH_2CO_2t$-Bu, $(i\text{-Pr})_2NEt$; (c) $BrCH_2CO_2t$-Bu, NaH; (d) NH_2NH_2, *t*-BuOH; (e) $BrCH_2CO_2Bn$, $(i\text{-Pr})_2NEt$; (f) H_2, Pd/C; (g) DCC, HOSu.

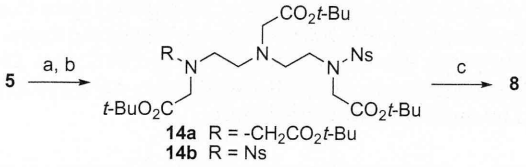

Scheme 2. Synthesis of DTPA precursor **8** via a global N-alkylation process using a Ns-protecting group. Reagents: (a) NsCl; (b) $BrCH_2CO_2t$-Bu, K_2CO_3; (c) $HSCH_2CO_2H$, LiOH.

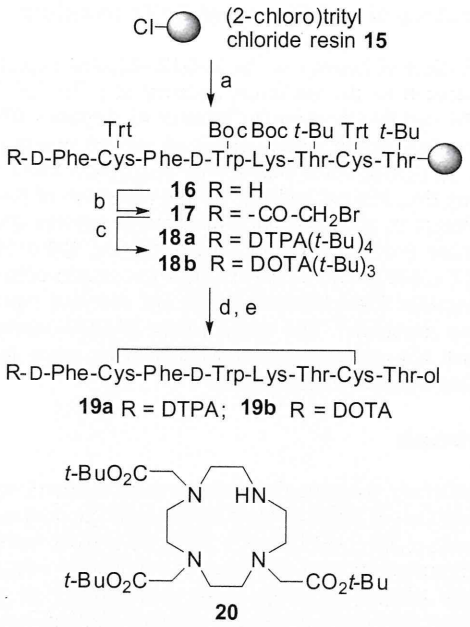

Scheme 3. Synthesis of DTPA- and DOTA-conjugated D-Phe-octreotides. Reagents: (a) Fmoc-based peptide synthesis; (b) $BrCH_2CO_2H$, DIC; (c) **8** for **18a**, or **20** for **18b**, $(i\text{-Pr})_2NEt$ (d) TFA/H_2O/1,2-ethanedithiol (EDT) (95:2.5:2.5) for **19a**, 1 M TMSBr, thioanisole/TFA, 1,2-ethanedithiol, *m*-cresol for **19b**; (e) NH_4OH (air oxidation).

26b,c, a Boc group was employed. This group can be cleaved by the standard TFA-based treatment in Fmoc chemistry (Scheme 4). After the construction of the protected peptide resin, the orthogonal Mtt group at the labeling position was cleaved off using 1,1,1,3,3,3-hexafluoropropan-2-ol (HFIP). The resulting ε-amino group was successively modified with bromoacetic acid followed by the reagent **8** to provide the fully protected DTPA–peptide resin **25**. Final deprotection, air-oxidation and HPLC purification afforded the expected DTPA-conjugated CXCR4 antagonists **26a,b**. This concise protocol facilitates the selection of chelating structure and position(s) on the peptide chain, and aids structure–activity relationship studies aimed at exploring the more potent peptide probes. For example, a 4-fluorobenzoyl modification at the N-terminus, which should increase CXCR4 antagonism,[28] was easily appended to the peptide using this protocol to give the modified peptide **26c**. The subsequent treatment with nonradioactive $InCl_3$ in acidic conditions provided the In-DTPA-labeled CXCR4 antagonists **27a–c**.

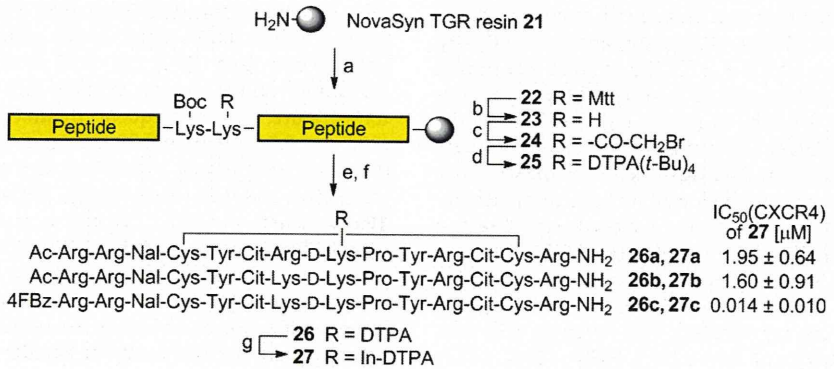

Scheme 4. Site-specific In-DTPA labeling of CXCR4 antagonists and biological activity. Reagents: (a) Fmoc-based peptide synthesis; (b) CH_2Cl_2/1,1,1,3,3,3-hexafluoro-2-propanol (HFIP)/2,2,2-trifluoroethanol (TFE)/triethylsilane (TES) (65:20:10:5); (c) $BrCH_2CO_2H$, DIC; (d) **8**, $(i\text{-Pr})_2NEt$; (e) TFA/H_2O/EDT (95:2.5:2.5); (f) NH_4OH (air oxidation); (g) $InCl_3$. *Abbreviations:* Mtt: 4-methyltrityl; Cit: L-citrulline, Nal: L-3-(2-naphthyl)alanine, 4FBz: 4-fluorobenzoyl.

2.3. Bioactivity of In-DTPA-labeled CXCR4 antagonists

The biological activity of the In-DTPA-labeled peptides **27a–c** was evaluated as the inhibitory potency of [^{125}I]-SDF-1-binding to CXCR4 membrane extracts (Scheme 4). Peptides **27a,b**, with an N-terminal acetyl group, exhibited similar potency towards CXCR4 [IC_{50}(**27a**) = 1.95 ± 0.64 μM, IC_{50}(**27b**) = 1.60 ± 0.91 μM], indicating that the Lys and Arg for the *i*-position of β-turn were both tolerant to the bioactivity. In contrast, peptide **27c** exerted much more potent inhibitory activity for the SDF-1 binding to CXCR4 [IC_{50}(**27c**) = 0.014 ± 0.010 μM]. These results of In-DTPA-labeled peptides **27a–c** coincided with our previous report on the unlabeled peptides.[28] The novel potent In-DTPA-labeled CXCR4 antagonist **27c** could be a promising imaging probe for CXCR4-expressing malignant cancer cells.[11]

3. Conclusions

In this study, we have established a novel synthetic method for the production of DTPA–peptide conjugates. The process includes facile solid-phase synthesis of a DTPA framework using a novel precursor substrate and site-specific conjugation using a highly acid-labile protecting group. Using a temporary Ns protecting group, the DTPA precursor **8** was obtained through two purification steps from commercially available diethylenetriamine. In addition, the on-resin incorporation of a bromoacetyl group into the specific free amino group followed by the addition of the nucleophilic DTPA precursors provided the expected DTPA–peptide conjugates with high purity. Taking advantage of secondary amine precursors of choice, these processes represent versatile methods to prepare a series of peptide conjugates, including DTPA and DOTA, for optimization of imaging probes. This conjugation method was applied to the preparation of DTPA-conjugates of octreotide and CXCR4 antagonist, which have been reported to effectively detect cancer cells. The peptide **27c** with highly potent inhibitory activity of SDF-1 binding to CXCR4 was obtained without any amino acid substitution to avoid multiple modifications on the amino groups. This peptide represents a promising lead compound as an imaging probe towards CXCR4-positive metastatic tumors.

4. Experimental

4.1. Synthesis

4.1.1. Bis(*tert*-butyl) 3,6-bis[(*tert*-butoxycarbonyl)methyl]-9-(*o*-nitrobenzenesulfonyl)-3,6,9-triazaundecanedioate (14a)

To diethylenetriamine **5** (0.540 mL, 5.00 mmol) in dehydrated EtOH (5 mL), *o*-NsCl (0.367 g, 1.67 mmol) was slowly added below 0 °C. After stirring for 2 h, EtOH was removed in vacuo. To dehydrated DMF (8 mL), K_2CO_3 (4.49 g, 32.5 mmol) and $BrCH_2CO_2t$-Bu (4.06 mL, 27.5 mmol) were added at 0 °C. The mixture was stirred overnight at room temperature, and filtered. The filtrate was concentrated under reduced pressure to give an oily residue, and the residue was dissolved in EtOAc (100 mL). The whole mixture was washed with saturated $NaHCO_3$, and was dried over $MgSO_4$. Concentration under reduced pressure followed by flash chromatography over silica gel with *n*-hexane–EtOAc gave compound **14a** as a yellow oil (0.81 g, 65%); ^{1}H NMR ($CDCl_3$, 500 MHz) δ 8.08–8.11 (1H, m), 7.64–7.69 (2H, m), 7.56–7.60 (1H, m), 4.24 (2H, s), 3.49 (2H, t, *J* = 6.9 Hz), 3.42 (4H, s), 3.30 (2H, s), 2.88 (2H, t, *J* = 6.6 Hz), 2.78 (2H, t, *J* = 6.9 Hz), 2.77 (2H, t, *J* = 6.9 Hz), 1.45 (27H, s), 1.36 (9H, s); ^{13}C NMR ($CDCl_3$, 500 MHz) δ 170.6 (3C), 168.0, 133.7, 133.2, 131.6 (2C), 130.9, 123.9, 82.0, 81.0, 80.9 (2C), 56.1 (3C), 53.3, 52.8, 52.4, 49.4, 46.7, 28.1 (9C), 27.9 (3C); HRMS (FAB) *m/z* calcd for $C_{34}H_{58}N_4O_{12}S$ ([M+H]$^+$): 746.3772, found 746.3779.

4.1.2. Bis(*tert*-butyl) 3,6-bis[(*tert*-butoxycarbonyl)methyl]-3,6,9-triazaundecanedioate (8)

To a solution of compound **14a** (0.216 g, 0.29 mmol) in DMF (0.726 mL), LiOH (0.128 g, 2.90 mmol) and mercaptoacetic acid (0.101 mL, 1.45 mmol) were added below 0 °C. After stirring for 2 h at room temperature, the mixture was concentrated under reduced pressure, and the residue was dissolved in $CHCl_3$. The whole reaction mixture was washed with saturated $NaHCO_3$, and was dried over Na_2SO_4. Concentration under reduced pressure followed by flash chromatography over silica gel with $CHCl_3$–MeOH gave compound **8** as a yellow oil (0.124 g, 77%); ^{1}H NMR ($CDCl_3$, 500 MHz) δ 3.39 (4H, s), 3.28 (4H, s), 2.72–2.82 (6H, m), 2.63 (2H, t, *J* = 5.4 Hz), 1.39 (9H, s), 1.38 (27H, s); ^{13}C NMR ($CDCl_3$, 500 MHz) δ 170.9, 170.7 (3C), 80.8 (4C), 55.9 (2C), 55.8 (2C), 52.4, 52.3, 51.3, 47.0, 28.2 (3C), 28.1 (9C); HRMS (FAB) *m/z* calcd for $C_{28}H_{54}N_3O_8$ ([M+H]$^+$): 560.3911, found 560.3910.

4.1.3. Standard procedure for solid-phase peptide synthesis

Protected peptide-resins were manually constructed by Fmoc-based solid-phase peptide synthesis. *t*-Bu ester for Asp and Glu; 2,2,4,6,7-pentamethyldihydrobenzofurane-5-sulfonyl (Pbf) for Arg; *t*-Bu for Thr and Tyr; Boc for Lys and Trp; Trt for Cys were employed for side-chain protection. Fmoc-amino acids were coupled using three equivalents of reagents [Fmoc-amino acid, 1,3-diisopropylcarbodiimide (DIC), and HOBt·H_2O] to the free amino group in DMF for 1.5 h. Fmoc deprotection was performed by 20% (v/v) piperidine in DMF (2 × 1 min, 1 × 30 min). The protected peptide resin was treated with a cocktail of deprotection reagents. After removal of the resin by filtration, the filtrate was poured into ice-cold dry Et_2O. The resulting powder was collected by centrifugation and washed with ice-cold dry Et_2O. The crude peptide was dissolved in H_2O, and the pH was adjusted to 8.0 with NH_4OH for disulfide bond formation. After air-oxidation for 1 d, the crude product was purified by preparative HPLC on a Cosmosil 5C18-ARII preparative column (Nacalai Tesque, Kyoto, Japan; 20 × 250 mm, flow rate 10 mL/min) to afford the expected peptides. All peptides were characterized by MALDI-TOF-MS (AXIMA-CFR plus, Shimadzu, Kyoto, Japan) and the purity was calculated as >95% by HPLC on a Cosmosil 5C18-ARII analytical column (Nacalai Tesque, 4.6 × 250 mm, flow rate 1 mL/min) at 220 nm absorbance.

4.1.4. Preparation of DTPA- and DOTA-conjugated octreotides (19a,b)

According to the procedure reported previously,[18] (2-chloro)trityl chloride resin **15** (214 mg, 1.4 mmol/g), Fmoc-Thr(*t*-Bu)-ol (345 mg, 0.9 mmol), and pyridine (0.145 mL, 1.8 mmol) were agitated for 21 h in dry CH_2Cl_2–DMF (1:1, 3.94 mL). The loading was determined by measuring the 290 nm UV absorption of the piperidine-treated sample (0.455 mmol/g). After the construction of the peptide chain (0.017 mmol scale) using a standard procedure, bromoacetic acid (23.6 mg, 0.17 mmol) with DIC (0.026 mL, 0.17 mmol) in CH_2Cl_2 was reacted with resin **16** for 2 h at room temperature. The subsequent treatment of **17** with amines **8** (29.0 mg, 0.51 mmol) and **20** (26.3 mg, 0.51 mmol) with $(i\text{-Pr})_2$NEt (0.009 mL, 0.51 mmol) in DMF for 12 h at room temperature provided **18a** and **18b**, respectively. Cleavage and deprotection of **18a** (72.5 mg) and **18b** (73.8 mg) was achieved using a TFA/1,2-ethandithiol (EDT)/H_2O (5 mL; 95:2.5:2.5) cocktail for 2 h at room temperature and by treatment with 1 M TMSBr-thioanisole/TFA in the presence of EDT/*m*-cresol (3.3 mL) for 2 h at 0 °C, respectively. After disulfide formation under air-oxidation conditions, the crude peptides were purified using the standard procedure, to afford the desired peptides **19a** (8.2 mg, 23%) and **19b** (9.5 mg, 26%) as white powders. Compound **19a**: MS (MALDI-TOF) *m/z* calcd for $C_{63}H_{89}N_{13}O_{19}S_2$ ([M+H]$^+$): 1395.6, found 1395.3. Compound **19b**:

MS (MALDI-TOF) m/z calcd for $C_{65}H_{93}N_{14}O_{17}S_2$ ($[M+H]^+$): 1405.6, found 1405.8.

4.1.5. Preparation of DTPA-conjugated CXCR4 antagonists (26a–c)

Protected peptide resins were manually constructed according to the standard procedure using NovaSyn TGR-resin **21** (96.2 mg, 0.025 mmol). 4-Methyltrityl (Mtt) group was employed for the protection of the D-Lys ε-amino group. The N-terminal amino group was acylated by treatment with Ac_2O (0.012 mL, 0.125 mmol)/pyridine (0.020 mL, 0.250 mmol) for 1 h at room temperature for peptides **26a,b**, and with 4-fluorobenzoic acid (17.5 mg, 0.125 mmol)/DIC (0.019 mL, 0.125 mmol)/HOBt·H_2O (19.2 mg, 0.125 mmol) for 1.5 h at room temperature for peptide **26c**. Subsequently, the resin **22** was treated with CH_2Cl_2/1,1,1,3,3,3-hexafluoropropan-2-ol (HFIP)/trifluoroethanol (TFE)/triethylsilane (TES) [65:20:10:5; 5 mL] for 2 h at room temperature. The DTPA group was incorporated using the identical procedure employed for the synthesis of the octreotide derivative **19a**. Treatment of the resins (**25a**: 178 mg, **25b**: 165 mg, **25c**: 162 mg) with a TFA/1,2-ethandithiol(EDT)/H_2O (95:2.5:2.5; 5 mL) cocktail for 2 h at room temperature followed by air oxidation and purification provided the peptides Compound **26a** (14.6 mg, 15.4%), **26b** (6.67 mg, 8.7%) and **26c** (7.4 mg, 9.5%) as white powders. Compound **26a:** MS (MALDI-TOF) m/z calcd for $C_{106}H_{165}N_{38}O_{28}S_2$ ($[M+H]^+$): 2482.2, found 2482.5. Compound **26b**: MS (MALDI-TOF) m/z calcd for $C_{106}H_{165}N_{36}O_{28}S_2$ ($[M+H]^+$): 2454.2, found 2453.9. Compound **26c**: MS (MALDI-TOF) m/z calcd for $C_{111}H_{166}FN_{36}O_{28}S_2$ ($[M+H]^+$): 2534.2, found 2533.8.

4.1.6. Indium chelating for CXCR4 antagonist probes (27a–c)

To a solution of peptides **26a–c** (8 mM in 0.1 N AcOH, **26a**: 45.9 μL, 0.37 μmol; **26b**: 48.4 μL, 0.39 μmol; **26c**: 48.8 μL, 0.39 μmol), $InCl_3$ (1 M in 0.02 N HCl, 50 μL) was added and the solution stirred for a further 30 min at room temperature. HPLC purification using a standard procedure provided the desired peptides **27a** (0.43 mg, 36.7%), **27b** (0.42 mg, 34.3%) and **27c** (0.38 mg, 30.3%) as white powders. Compound **27a**: MS (MALDI-TOF) m/z calcd for $C_{106}H_{165}InN_{38}O_{28}S_2$ ($[M+H]^+$): 2597.1, found 2596.9. Compound **27b**: MS (MALDI-TOF) m/z calcd for $C_{106}H_{165}InN_{36}O_{28}S_2$ ($[M+H]^+$): 2569.1, found 2569.1. Compound **27c**: MS (MALDI-TOF) m/z calcd for $C_{111}H_{166}FInN_{36}O_{28}S_2$ ($[M+H]^+$): 2649.1, found 2649.0.

4.2. Evaluation of [^{125}I]-SDF-1 binding and displacement

For ligand binding, the CXCR4 membrane was incubated with 0.5 nM of [^{125}I]-SDF-1 and increasing concentrations of compounds **27a–c** in binding buffer [50 mM HEPES (pH 7.4), 5 mM $MgCl_2$, 1 mM $CaCl_2$ and 0.1% BSA in H_2O] for 1 h at room temperature. The reaction mixtures were filtered through GF/B filters (Perkin-Elmer, Wellesley, MA) pretreated with 0.1% polyethyleneimine. The filter plate was washed with wash buffer [50 mM HEPES (pH 7.4), 500 mM NaCl and 0.1% BSA in H_2O] and the bound radioactivity was measured by TopCount (Packard, Meriden, CT). Inhibitory activity of test compounds was determined based on the inhibition of [^{125}I]-SDF-1 binding to the CXCR4 receptor (IC_{50}).

Acknowledgments

This work is supported by Grants-in-Aid for Scientific Research and Molecular Imaging Research Program from the Ministry of Education, Culture, Sports, Science, and Technology of Japan. R.M. is grateful for Research Fellowships from the JSPS for Young Scientists.

Supplementary data

Supplementary data associated with this article can be found, in the online version, at doi:10.1016/j.bmc.2011.03.059.

References and notes

1. Lee, S.; Xie, J.; Chen, X. *Chem. Rev.* **2010**, *110*, 3087.
2. De León-Rodríguez, L. M.; Kovacs, Z. *Bioconjugate Chem.* **2008**, *19*, 391.
3. Mier, W.; Hoffend, J.; Krmer, S.; Schuhmacher, J.; Hull, W. E.; Eisenhut, M.; Haberkorn, U. *Bioconjugate Chem.* **2005**, *16*, 237.
4. Lewis, M. R.; Shively, J. E. *Bioconjugate Chem.* **1998**, *9*, 72.
5. Heppeler, A.; Froidevaux, S.; Mäcke, H. R.; Jermann, E.; Powell, P.; Henning, M. *Chem. Eur. J.* **1999**, *5*, 1974.
6. De León-Rodriguez, L. M.; Kovacs, Z.; Dieckmann, G. R.; Sherry, A. D. *Chem. Eur. J.* **2004**, *10*, 1149.
7. Wild, D.; Wicki, A.; Mansi, R.; Béhé, M.; Keil, B.; Bernhardt, P.; Christofori, G.; Ell, P. J.; Mäcke, H. R. *J. Nucl. Med.* **2010**, *51*, 1059, and the references therein.
8. De Jong, M.; Breeman, W. A.; Bakker, W. H.; Kooij, P. P.; Bernard, B. F.; Hofland, L. J.; Visser, T. J.; Srinivasan, A.; Schmidt, M. A.; Erion, J. L.; Bugaj, J. E.; Mäcke, H. R.; Krenning, E. P. *Cancer Res.* **1998**, *58*, 437.
9. Hnatowich, D. J.; Layne, W. W.; Childs, R. L. *Int. J. Appl. Radiat. Isot.* **1982**, *33*, 327.
10. Wang, S.; Luo, J.; Lantrip, D. A.; Waters, D. J.; Mathias, C. J.; Green, M. A.; Fuchs, P. L.; Low, P. S. *Bioconjugate Chem.* **1997**, *8*, 673.
11. Reilly, R.; Lee, N.; Houle, S.; Law, J.; Marks, A. *Appl. Radiat. Isot.* **1992**, *43*, 961.
12. Hnatowich, D. J.; Layne, W. W.; Childs, R. L.; Lanteigne, D.; Davis, M. A.; Griffin, T. W.; Doherty, P. W. *Science* **1983**, *220*, 613.
13. Van Hagen, P. M.; Breeman, W. A. P.; Bernard, H. F.; Schaar, M.; Mooij, C. M.; Srinivasan, A.; Schmidt, M. A.; Krenning, E. P.; De Jong, M. *Int. J. Cancer* **2000**, *90*, 186.
14. Arano, Y.; Uezono, T.; Akizawa, H.; Ono, M.; Wakisaka, K.; Nakayama, M.; Sakahara, H.; Konishi, J.; Yokoyama, A. *J. Med. Chem.* **1996**, *39*, 3451.
15. A portion of this study was reported in a preliminary communication: Masuda, R.; Ohno, H.; Oishi, S.; Fujii, N. In *Pepide Science*, Okamoto, Ed.; 2009, p 159.
16. Peterson, J. J.; Pak, R. H.; Meares, C. F. *Bioconjugate Chem.* **1999**, *10*, 316.
17. Hidai, Y.; Kan, T.; Fukuyama, T. *Chem. Pharm. Bull.* **2000**, *48*, 1570.
18. Arano, Y.; Akizawa, H.; Uezono, T.; Akaji, K.; Ono, M.; Funakoshi, S.; Koizumi, M.; Yokoyama, A.; Kiso, Y.; Saji, H. *Bioconjugate Chem.* **1997**, *8*, 442.
19. Lewis, J. S.; Anderson, C. J. *Methods Mol. Biol.* **2007**, *386*, 227.
20. Albert, R.; Smith-Jones, P.; Stolz, B.; Simeon, C.; Knecht, H.; Bruns, C.; Pless, J. *Bioorg. Med. Chem. Lett.* **1998**, *8*, 1207.
21. Müller, A.; Homey, B.; Soto, H.; Ge, N.; Catron, D.; Buchanan, M. E.; McClanahan, T.; Murphy, E.; Yuan, W.; Wagner, S. N.; Barrera, J. L.; Mohar, A.; Verástegui, E.; Zlotnik, A. *Nature* **2001**, *410*, 50.
22. Hermann, P. C.; Huber, S. L.; Heeschen, C. *Cell Cycle* **2008**, *7*, 188.
23. Oishi, S.; Masuda, R.; Evans, B.; Ueda, S.; Goto, Y.; Ohno, H.; Hirasawa, A.; Tsujimoto, G.; Wang, Z.; Peiper, S. C.; Naito, T.; Kodama, E.; Matsuoka, M.; Fujii, N. *ChemBioChem* **2008**, *9*, 1154.
24. Nishizawa, K.; Nishiyama, H.; Oishi, S.; Tanahara, N.; Kotani, H.; Mikami, Y.; Toda, Y.; Evans, B. J.; Peiper, S. C.; Saito, R.; Watanabe, J.; Fujii, N.; Ogawa, O. *Int. J. Cancer* **2010**, *127*, 1180.
25. Hanaoka, H.; Mukai, T.; Tamamura, H.; Mori, T.; Ishino, S.; Ogawa, K.; Iida, Y.; Doi, R.; Fujii, N.; Saji, H. *Nucl. Med. Biol.* **2006**, *33*, 489.
26. Tamamura, H.; Omagari, A.; Oishi, S.; Kanamoto, T.; Yamamoto, N.; Peiper, S. C.; Nakashima, H.; Otaka, A.; Fujii, N. *Bioorg. Med. Chem. Lett.* **2000**, *10*, 2633.
27. Stephenson, K. A.; Banerjee, S. R.; McFarlane, N.; Boreham, D. R.; Maresca, K. P.; Babich, J. W.; Zubieta, J.; Valliant, J. F. *Can. J. Chem.* **2005**, *83*, 2060.
28. Tamamura, H.; Hiramatsu, K.; Mizumoto, M.; Ueda, S.; Kusano, S.; Terakubo, S.; Akamatsu, M.; Yamamoto, N.; Trent, J. O.; Wang, Z.; Peiper, S. C.; Nakashima, H.; Otaka, A.; Fujii, N. *Org. Biomol. Chem.* **2003**, *1*, 3663.


1. 悪性腫瘍の分子イメージングのための新しい分子プローブの設計

[1]京都大学医学部附属病院 RI 実験施設、[2]京都大学大学院薬学研究科　上田真史[1]・天満敬[2]・佐治英郎[2]

1．はじめに

悪性腫瘍を対象とした分子イメージングプローブである ^{18}F-FDG は、腫瘍の病期診断、再発・転移診断など、主として腫瘍の存在の有無やサイズを評価するために用いられている。一方で、浸潤・転移能や治療反応性など、腫瘍の性質は非常に多様性に富むことが知られており、腫瘍の性状把握・質的診断を可能とする分子イメージングプローブがポスト FDG として期待されている。また近年、抗体医薬・タンパク医薬の発展には目覚しいものがあり、抗体やタンパク質・ペプチドの高い生理活性に着目してそれらを母体とした分子プローブ開発も注目を集めている。

2．機能性ユニットカップリング型分子プローブ

^{18}F-FDG は ^{18}F 標識されたブドウ糖類似体であり、^{11}C-PIB はβアミロイド結合性を有するチオフラビンT類似体の ^{11}C 標識体である。このように従来のイメージングプローブは、目的とする性質を有する化合物に RI 標識を施したある一つのかたまり（単一分子）として捉えられるのが一般的であった。これに対し我々は、イメージングプローブを「標的認識ユニット」「リンカーユニット」「シグナル放出ユニット」の各ユニットの集合体として捉える「機能性ユニットカップリング型分子プローブ」という新概念に基づく分子プローブ設計を行っている（図 1）。この方法では、イメージング対象に発現している標的分子や利用する撮像装置に応じて最適なユニットを選択することで、種々のイメージング標的・装置に対応可能な汎用性の高い分子プローブの開発が可能となる。さらに、「標的認識ユニット」と「クリアランスの速い低分子シグナル放出ユニット」のカップリングをインビボ（*in vivo*）で行うことにより体内動態を制御し、投与早期での高コントラスト画像の取得・被ばく線量の低減を実現することもできる。本稿ではこの概念に基づいて設計した、膜結合型マトリクス分解酵素（membrane type 1 matrix metalloproteinase;

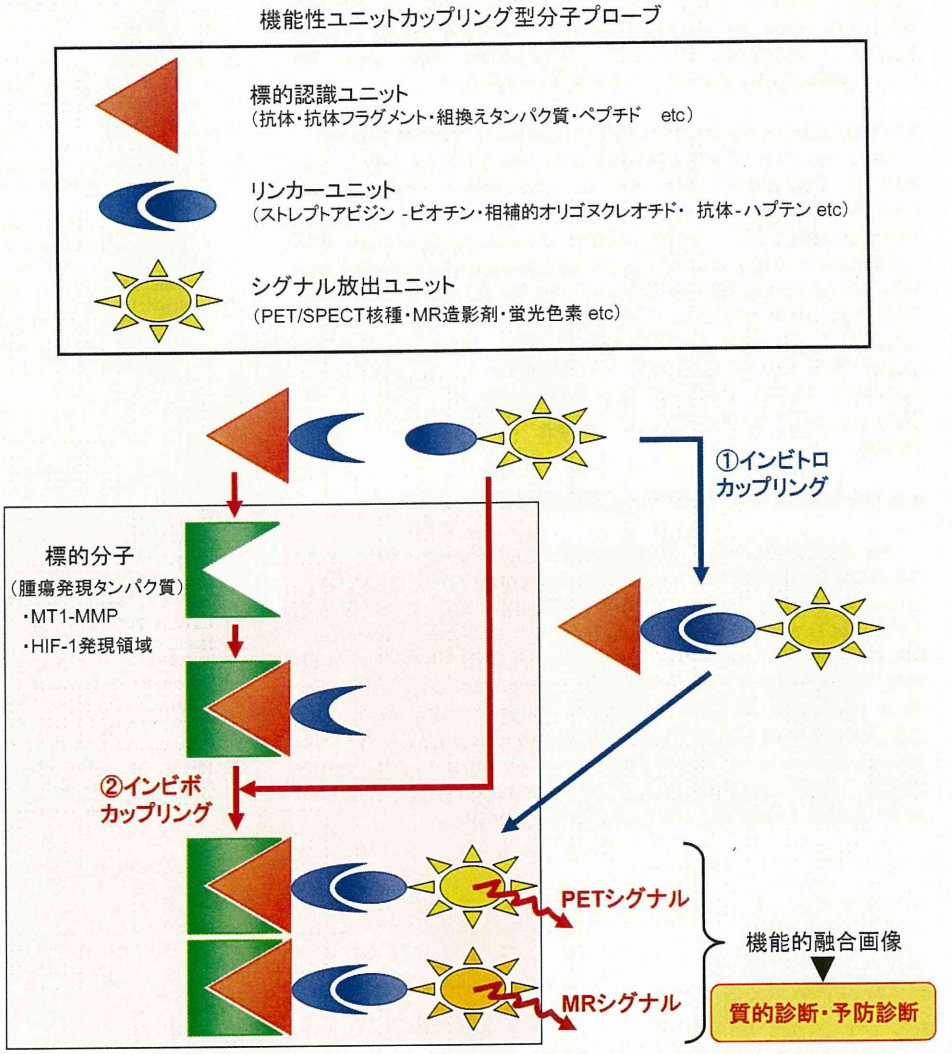

図1　機能性ユニットカップリング型プローブを利用したイメージングの概念図

MT1-MMP）標的イメージングプローブおよび低酸素誘導因子（hypoxia-inducible factor-1; HIF-1）存在領域イメージングプローブの研究成果を紹介する。

3. MT1-MMP 標的分子イメージングプローブの開発

MT1-MMP は、乳がんを始めとした種々の腫瘍において MMP-2 の活性化を介した悪性度との高い関連性が示されている。さらに、分泌型酵素である MMP-2 とは異なり、膜結合型でその発現が腫瘍細胞の細胞膜上に限局していることから、腫瘍の存在位置を確実に把握しつつ悪性度診断（質的診断）を同時に行うことができる非常に有望なイメージング標的分子である。

MT1-MMP をイメージングするため、我々は、当該タンパク質の細胞膜外領域に存在し、生体内での3次元構造・代謝調節機構を踏まえ認識されやすいと考えられるペプチド配列をエピトープとする抗 MT-1MMP モノクローナル抗体（mAb）を標的認識ユニットとして選択した[1]。さらに、ストレプトアビジン－ビオチンの高親和性結合に着目し、ストレプトアビジン（SAV）をリンカーユニットとして抗体に導入したプローブ anti-MT1-MMP mAb-SAV を構築し、それに結合性を有するシグナル放出ユニットである放射性ヨウ素標識ビオチン誘導体（3-[$^{123/125}$I]iodobenzoyl)norbiotinamide; $^{123/125}$I-IBB）の合成も行った。まず、インビトロカップリングにより両者を直接結合させたプローブを用いて標的認識ユニットの有効性を評価したところ、MT1-MMP 発現細胞に高く取り込まれること、インビボで腫瘍集積性を示すことを見出し、選択した抗体が標的認識ユニットとして有効に機能することを明らかとした。次に、抗体の血液クリアランスの遅さを克服し、投与早期で良好な画像コントラストを達成するため、anti-MT1-MMP mAb-SAV を投与してから 72 時間後に ^{125}I-IBB を投与するインビボカップリングを検討したところ、投与3時間後における腫瘍血液比は直接結合体（インビトロカップリング）の場合の 30 倍以上であることを認めた[2]。そこで、^{123}I-IBB を投与後、SPECT を用いて経時的に撮像を行ったところ、投与3時間後から明瞭に腫瘍が描出された（図2）[2]。さらに、免疫組織化学的検討の結果、腫瘍内の放射能局在は MT1-MMP 発現部位と一致することを認めた。これらの結果から、ユニットカップリング型プローブの設計概念に基づいて構築した anti-MT1-MMP mAb-SAV と ^{123}I-IBB を用いてインビボカップリング SPECT 撮像を行うことにより、MT1-MMP 発現腫瘍の投与早期イメージングが可能となることを見出した。

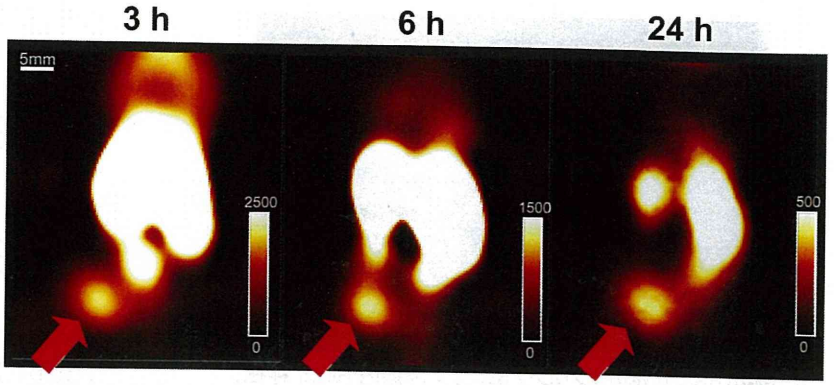

図2　インビボカップリング法による MT1-MMP 発現腫瘍の経時的 SPECT 画像
（矢印が腫瘍で、投与3時間後から明瞭に描出されている）

4. HIF-1 存在領域イメージングプローブの開発

HIF-1 は低酸素領域でのみ安定に存在する転写因子であり、糖代謝・血管新生・浸潤・転移に関与する種々のタンパク質発現を亢進させて腫瘍の悪性化や治療抵抗性に関与することが知られていることから、腫瘍内での HIF-1 存在量やその局在を同定できる分子プローブが開発できれば、腫瘍の性状把握・悪性度診断・予後予測に有用な情報を得ることが可能となる。また、HIF-1 が安定に存在しうる酸素分圧の閾値は一定ではなく、組織によって異なることが報告されている。すなわち HIF-1 は、生体組織が酸素不足を感じる生物学的低酸素領域に存在しており、その領域は酸素分圧が 10 mmHg 以下のいわゆる物理的低酸素領域と完全には一致しないことから、^{18}F-FMISO など既存の低酸素プローブとは別のコンセプトに基づくプローブ開発が必要となる。

HIF-1 はαサブユニット（HIF-1α）とβサブユニットからなる転写因子で、通常酸素環境下では HIF-1α は分解される一方、低酸素環境下では安定に存在することで転写活性を調節して

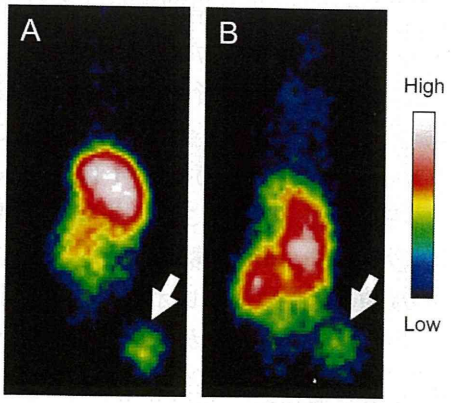

図3　POS と ^{123}I-IBB を用いたインビトロカップリング法（A：投与 24 時間後）およびインビボカップリング法（B：投与 6 時間後）による腫瘍内 HIF-1 存在領域（矢印）のプラナー画像

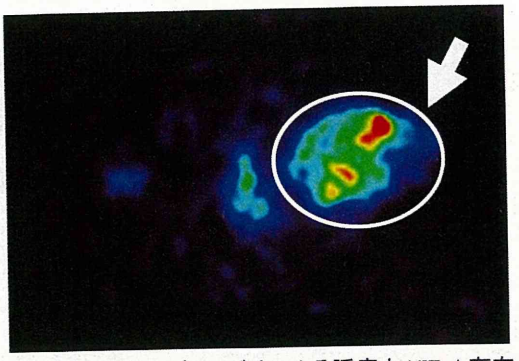

図4　インビボカップリング法による腫瘍内 HIF-1 存在領域(矢印)の PET 画像(投与 3 時間後に撮像)

いる。そこで我々はその分解機構に着目し、HIF-1α と同じメカニズムで分解・安定化の制御を受けるプローブを構築し、HIF-1 存在領域のイメージングの可能性について検討を行った。

HIF-1α の通常酸素環境下での分解には、タンパク質中の酸素依存的分解配列（oxygen-dependent degradation domain; ODD）が関与することが報告されている。そこで、ODD の中でも酸素依存的分解制御に必須のアミノ酸配列を選別し、それに細胞膜透過配列(protein transduction domain; PTD)および SAV 単量体を融合させた新規タンパク質 PTD-ODD-SAV（POS）を構築した。POS と ^{125}I-IBB をインビトロカップリングさせて細胞に処置したところ、通常酸素環境下（20%O_2）よりも低酸素環境下（0.1%O_2）で高い放射能集積を認めた。また、担がんマウスに投与して体内動態を検討したところ、投与 24 時間後で明瞭な腫瘍の画像化に成功し（図 3A）、そのときの放射能集積量および局在が HIF-1 転写活性や存在領域と一致することを認めた[3]。これらの結果から、POS が HIF-1 存在領域を対象とした標的認識ユニットとして有効に機能することが明らかとなった。

そこで次に、投与早期における HIF-1 存在領域イメージングを達成するためのインビボカップリング法の利用について検討を行った。POS を担がんマウスに投与し、インビトロカップリングの際に明瞭に腫瘍が描出された 24 時間後から ^{125}I-IBB を投与し、体内動態を経時的に調べたところ、投与 6 時間後で腫瘍に集積した放射能は非投与群の 30 倍以上であった。また、その集積は過剰量のビオチン投与によって抑制されたことから、^{125}I-IBB が所期の通り、POS の SAV 部分とインビボでカップリングすることが示された[4]。さらに、^{123}I-IBB を投与後、経時的にプラナー撮像を行ったところ、投与 6 時間後で明瞭に腫瘍が描出された（図 3B）[4]。これは、インビトロカップリングさせたプローブを投与してから 24 時間後と同等のコントラストの画像であり、POS と ^{123}I-IBB を用いるインビボカップリング法により、腫瘍内 HIF-1 存在領域の投与早期イメージングが可能となることを見出した。

このように、投与早期に高コントラスト画像を得られるイメージング法は、短半減期核種の利用が多い PET においては高い有効性が期待される。そこでこの概念を PET に応用すべく、放射性フッ素標識ビオチン誘導体（(4-[^{18}F]fluorobenzoyl)norbiotinamide; ^{18}F-FBB）を新規に設計・合成し、インビボカップリング PET に関する検討を行った。POS 投与 24 時間後に ^{18}F-FBB を投与して体内動態を経時的に調べたところ、投与 3 時間後で非投与群の 20 倍以上の放射能が腫瘍に集積し、その集積は過剰量のビオチン投与によって 80%以上抑制された。PET 撮像を行ったところ、投与 3 時間後で明瞭に腫瘍が描出され（図 4）、その放射能集積量および局在が HIF-1 転写活性や存在領域と一致することを認めた[5]。このようにインビボカップリング法は、短半減期核種を利用する PET の場合でも有効に機能することが明らかとなった。

5. おわりに

本稿では、「機能性ユニットカップリング型分子プローブ」の概念とその実用例として、腫瘍の転移能や低酸素状態といった性状を把握しうる分子プローブを紹介した。今後、この概念に基づき、多種多様ながんの性状それぞれを把握し得る「標的認識ユニット」および各モダリティに対応した「シグナル放出ユニット」を組み合わせることで、がんの性状をマルチモーダルに捉え得る分子プローブの効率的な開発が可能となる。それらの分子プローブは、悪性腫瘍の存在を単に検出するのみならず、質的診断に基づく治療方針の最適化にも大きく貢献することが期待できる。

6. 文献

1) Temma T, et al: Biol Pharm Bull 32: 1272–1277, 2009
2) Sano K, et al: Biol Pharm Bull 33: 1589–1595, 2010
3) Kudo T, et al: J Nucl Med 50: 942–949, 2009
4) Ueda M, et al: Eur J Nucl Med Mol Imaging 37: 1566–1574, 2010
5) Kudo T, et al: Mol Imaging Biol, in press

Multimodal nonlinear optical imaging of atherosclerotic plaque development in myocardial infarction-prone rabbits

Alex C. T. Ko,[a,*] Andrew Ridsdale,[b] Michael S. D. Smith,[a] Leila B. Mostaço-Guidolin,[a] Mark D. Hewko,[a] Adrian F. Pegoraro,[b] Elicia K. Kohlenberg,[a] Bernie Schattka,[a] Masashi Shiomi,[c] Albert Stolow,[b] and Michael G. Sowa[a]

[a]National Research Council Canada, Institute for Biodiagnostics, 435 Ellice Avenue, Winnipeg, Manitoba, Canada R3B 1Y6
[b]National Research Council Canada, Steacie Institute for Molecular Sciences, 100 Sussex Drive, Ottawa, Ontario, Canada K1A 0R6
[c]Kobe University School of Medicine, Institute of Experimental Animals, 7-5-1, Kusunoki-cho, Chuo-ku, Kobe 650-0017, Japan

Abstract. Label-free imaging of bulk arterial tissue is demonstrated using a multimodal nonlinear optical microscope based on a photonic crystal fiber and a single femtosecond oscillator operating at 800 nm. Colocalized imaging of extracellular elastin fibers, fibrillar collagen, and lipid-rich structures within aortic tissue obtained from atherosclerosis-prone myocardial infarction-prone Watanabe heritable hyperlipidemic (WHHLMI) rabbits is demonstrated through two-photon excited fluorescence, second harmonic generation, and coherent anti-Stokes Raman scattering, respectively. These images are shown to differentiate healthy arterial wall, early atherosclerotic lesions, and advanced plaques. Clear pathological changes are observed in the extracellular matrix of the arterial wall and correlated with progression of atherosclerotic disease as represented by the age of the WHHLMI rabbits. © *2010 Society of Photo-Optical Instrumentation Engineers.* [DOI: 10.1117/1.3353960]

Keywords: atherosclerosis; nonlinear optical microscopy; photonic crystal fiber; coherent anti-Stokes Raman scattering; two-photon excited fluorescence; second harmonic generation.

Paper 09412LR received Sep. 18, 2009; revised manuscript received Jan. 27, 2010; accepted for publication Feb. 10, 2010; published online Mar. 12, 2010.

Atherosclerosis is the primary cause of heart disease, stroke, and lower limb amputation worldwide. It is a progressive disease characterized by chronic inflammation of injured intima and is associated with fatty plaque deposits in the arteries.[1,2] Early atherosclerosis cannot be reliably detected by current clinical methods, therefore the disease is often overlooked until at a more advanced stage. The development of new tools that provide greater sensitivity and specificity for early detection and differentiation of atherosclerotic plaques would help our understanding of early disease and help establish preventative regimens that would slow disease progression.

Recently, nonlinear optical (NLO) microscopy has emerged as a powerful tool for tissue imaging. It is a label-free method with high sensitivity and specificity for major extracellular molecules. Its optical sectioning capability presents a means of 3-D *in vivo* imaging that would be useful in the context of atherosclerosis diagnostics. Several studies have demonstrated imaging of arterial tissue using NLO microscopy,[3–6] including studies imaging atherosclerotic lesions using a multimodal coherent anti-Stokes Raman Scattering (CARS) microscope based on two tightly synchronized Ti:sapphire lasers and a swine animal model.[6,7] In our study, we demonstrate label-free visualization of the extracellular matrix of arterial lumen and atherosclerotic plaques using a photonic crystal fiber (PCF)-based multimodal NLO microscope employing only a single femtosecond oscillator. Two-photon excited autofluorescence (TPEF) is able to specifically image extracellular elastin fibers, second harmonic generation (SHG), type-1 collagen fibrils, and CARS lipid-rich structure or extracellular lipids droplets in unstained bulk intact tissue, indicating the methods are particularly suited to understanding the role and interplay between these key extracellular molecules involved in plaque development.

PCF-based CARS was recently reported as an alternative CARS imaging method in biology.[8,9] Because it only requires a single femtosecond laser, PCF-based CARS can be easily integrated into existing multiphoton microscopes with minimal reconfiguration, and provides CARS capability at a relatively low cost. Its portability and its future potential of being developed into an all-fiber, single-laser-based CARS imaging system are better than a conventional dual-color system. From a clinical research point of view, this CARS configuration is better adapted to being implemented in a surgical environment.

Colocalized elastin/type-1 collagen lipid imaging of bulk arterial tissues freshly harvested from WHHLMI rabbits is achieved at micron resolution using a home-built NLO microscope. The TPEF and SHG signals are obtained using the femtosecond pump pulses, with the CARS signal being generated by spatially and temporally overlapping the pump pulse with the Stokes pulse produced in a PCF that is synchronously pumped by the same femtosecond laser. Our goals in this study are to investigate the potential of a PCF-based multimodal NLO imaging system for bulk tissue imaging and for extracting biomorphological information related to atherosclerotic lesion development in myocardial infarction-prone rabbits.

Figure 1 illustrates our PCF-based multimodal NLO imaging system used in this study. A green-pumped Ti:sapphire oscillator (Tsunami, Spectra-Physics, Mountain View, California) is the laser source, and the output wavelength is centered at 800 nm with a pulse duration of 100 fs, an 80-MHz repetition rate, and average output power of 1 W. The femtosecond pulses from the Ti:sapphire oscillator first pass through a Faraday isolator and then a pair of GTI chirp mirrors (Layertec GmbH, Germany). These mirrors are used to compensate for the large group velocity dispersion (GVD) caused by the Faraday isolator. The femtosecond pulses are then split

*Address all correspondence to: Alex C.T. Ko. Tel: 204-984-4622; Fax: 204-984-5472; E-mail: alex.ko@nrc-cnrc.gc.ca

1083-3668/2010/15(2)/020501/3/$25.00 © 2010 SPIE

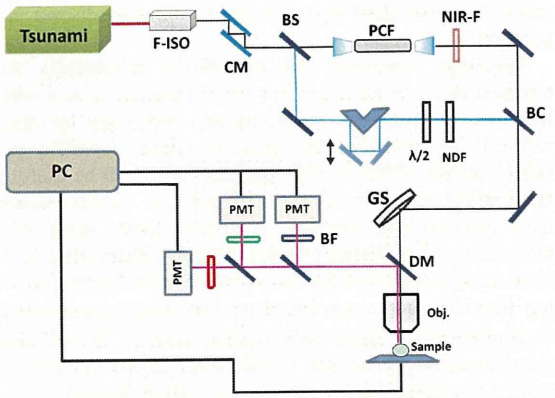

Fig. 1 Schematic of the inhouse-built nonlinear optical laser-scanning microscope with the Stokes pulses being generated in PCF, which is synchronously pumped by the same Ti:sapphire laser that provides the pump pulse. F-ISO: Faraday isolator; CM: chirp laser mirrors; BS: beamsplitter; NIR-F: near-IR filter; BC: beam combiner; GS: galvo scanner; DM: dichroic mirror; OBJ: objective lens; BF: bandpass filter; NDF: neutral density filter; and $\lambda/2$: half waveplate.

into two beams at a beamsplitter. The reflected "pump" pulse is transmitted through a series of optical components outlined in Fig. 1, while the transmitted pulse is coupled into a PCF (NL-1.4.775-945, NTK Photonics A/S, Denmark) through a 40× objective lens to generate a supercontinuum (SC). This SC emission is recollimated through a 20× objective lens and filtered through a near-infrared (NIR) filter to select only the NIR portion (950 nm$<\lambda<$1150 nm), which is then used as the Stokes pulses for generating the CARS signal. The pump and Stokes pulses are combined at a beam combiner and sent collinearly into the microscope assembly. Epi-NLO signals are collected through an Olympus 20×, 0.75-NA objective lens (UPlanSApo) and then detected using nondescanned PMT modules (H-9656, Hamamatsu, Bridgewater, New Jersey). Spectral separation of TPEF, SHG, and CARS signals is achieved through an array of dichroic lenses and bandpass filters. A 40×, 0.8-NA, water immersion objective lens (Olympus LUMPlanFl/lR) is used to collect tissue images of greater spatial and depth resolution in selected regions of interest. Typically, 25 mW of pump and 8 mW of Stokes are used at the sample for imaging. ScanImage software[10] (Cold Spring Harbor Laboratory, New York) is used for image acquisition and controlling translational stage movement during depth imaging. For images shown, total pixel dwell time is 21 μs from an average of four scans. ImageJ ver 1.42b (National Institutes of Health, Bethesda, Maryland) is used for image viewing and post-processing.

Animal studies were approved by the local Animal Care Committee of the National Research Council of Canada. This study uses the myocardial infarction-prone Watanabe heritable hyperlipidemic (WHHLMI) rabbit model[11] which highly resembles human in lipoprotein metabolism compared to other models, and develops atherosclerotic plaques rapidly due to a hereditary defect in low-density lipoprotein processing. Seven WHHLMI rabbits were used for this study. Six rabbits were each sacrificed at 4, 10, 11, 16, 18, and 22 months, whereas the seventh rabbit died naturally at the age of 24 months. For each rabbit, fresh aorta was dissected from the ascending aorta to the external iliac artery, rinsed in heparinized saline,

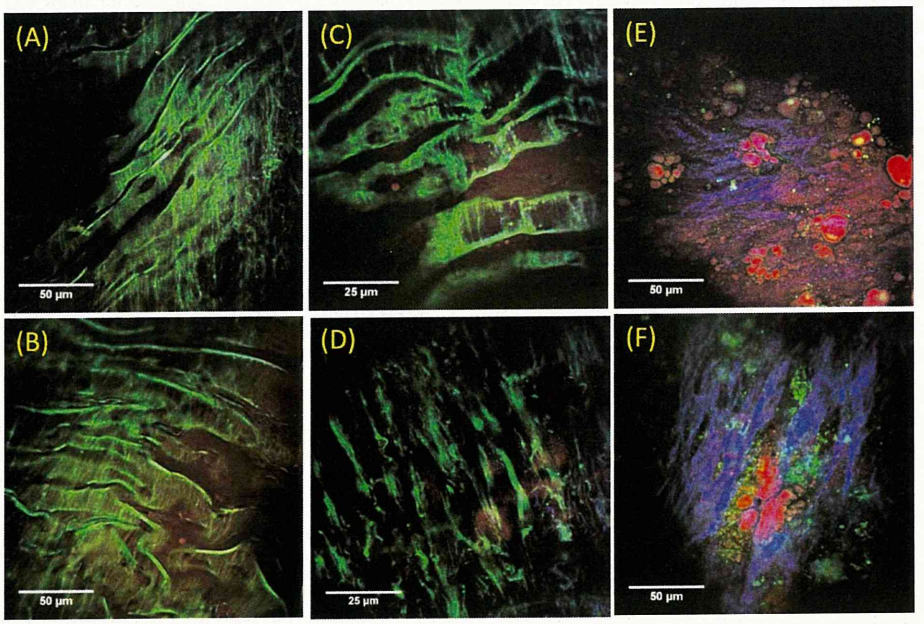

Fig. 2 Representative epi-NLO images collected from healthy arterial lumen on a (a) 4-month-old and (b) 10-month-old WHHLMI rabbit using 20× air objective lens, and on a 4-month-old rabbit using 40× WI lens at (c) lumen surface and (d) ~20 μm depth from surface. Representative epi-NLO images of arterial lumen surface obtained from (e) an early atherosclerotic lesion and (f) an advanced atherosclerotic lesion using 20× air lens. Green:TPEF (elastin or other fluorescent particles). Blue:SHG (collagen). Red:CARS (lipid-rich structure). (Color online only.)

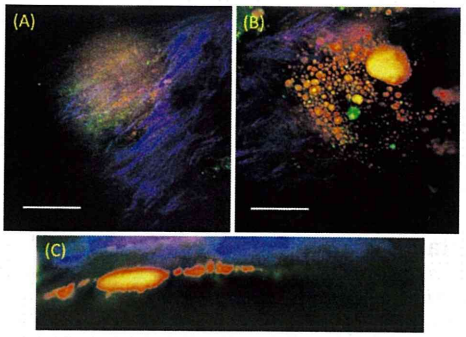

Fig. 3 Epi-NLO images of an advanced plaque obtained at (a) ~10 μm depth, (b) ~60 μm depth from the lumen surface, and (c) the side-view of the image stack showing a collagen cap overlaying lipid-rich bulk. Blue:SHG (collagen), and red/orange:CARS (lipid-rich structure). The scale bar is 25 μm. (Color online only.)

and then subdivided into ~20- to 30-mm sections. Each section was cut open longitudinally, exposing the luminal surface. The samples were placed in petri dishes with the luminal surface facing up. Phosphate buffered saline solution was applied to the samples periodically to maintain hydration. Healthier arterial lumen from the 4-month-old rabbit showed mostly smooth and flat surfaces with occasional raised lesions. Plaque-covered luminal surfaces were observed in rabbits aged 10 to 24 months with the burden increasing with age. This observation is consistent with the result reported on progressive atherosclerosis in the WHHLMI rabbits.[12]

Representative epi-NLO images of healthy luminal surfaces measured on 4- and 10-month-old rabbits are shown in Figs. 2(a) and 2(b), respectively. Near the surface of the vessel wall, a layer of membrane structure giving rise to strong TPEF signal (shown in green) is evident. At a depth of approximately 20 μm, a different fibril structure appears in the TPEF images with the orientation of these structural fibers running nearly perpendicular to that of the membrane layer detected closer to the surface. [Fig. 2(d)]. The membrane-shaped structure shown in Figs. 2(a)–2(c) is consistent with internal elastic lamina in arterial tunica intima, and the fibril structure shown in Fig. 2(d) is believed to be the bulk elastin network in arterial tunica media. A representative NLO image acquired from the surface of an early atherosclerotic lesion found on the arterial wall of the 10-month-old rabbit is illustrated in Fig. 2(e). Unlike in the images acquired from healthy luminal surfaces, no internal elastic lamina is visible. Instead, scattered collagen fibers, accumulated lipid-rich structures, and nonfibrous fluorescent structures emerged from the image. Images acquired from advanced plaque reveal lumen pathology similar to those of early lesions, with differences in collagen fibril morphology and denser systems of nonfibrous fluorescent structures. Older, more advanced plaques show thicker and directional collagen fibrils, as seen in Fig. 2(f), whereas early and midstage lesions show thinner and less directional collagen fibrils [Fig. 2(e)]. Figure 2(e) also shows the accumulation of extracellular lipid aggregates and the early formation of collagen fibrils within a lesion.

Depth scanning of an advanced plaque on a 22-month-old rabbit artery shows a thin collagen fibril layer overlaying a pool of lipid debris, a typical pathology of a rupture-prone atherosclerotic plaque. Figures 3(a) and 3(b) are two focal depth images obtained from the same location on an advanced plaque at depths approximately 10 and 60 μm respectively from the lumen surface. In Fig. 3(c) a reconstructed side-view image representing a depth profile of this particular plaque shows a collagen layer on top of a lipid-rich pool.

In conclusion, we demonstrated multimodal nonlinear optical imaging of bulk arterial tissue from WHHLMI rabbits using a cost-effective PCF-based nonlinear optical microscope. Epi-NLO imaging of unsectioned arteries allowed label-free visualization of extracellular components relevant to the development of atherosclerosis. Clear differences in the surface biochemical morphology were observed between healthy artery wall, early atherosclerotic lesions, and advanced plaques. In particular, differences in collagen fibril structures were noted between early and advanced lesions. Such changes in collagen morphology detected by SHG may provide a clinical measure for differentiating plaque burden.

Acknowledgment

The authors acknowledge Vijay Iyer for the assistance provided in using ScanImage, and Jeri Friesen for her assistance in preparing figures. This work was supported by the National Research Council Canada, Genomics and Health Initiative.

References

1. P. Libby, "Atherosclerosis: disease biology affecting the coronary vasculature," *Am. J. Cardiol.* **98**[suppl], 3Q–9Q (2006).
2. G. K. Hansoon, "Inflammation, atherosclerosis, and coronary artery disease," *N. Engl. J. Med.* **352**, 1685–1695 (2005).
3. A. Zoumi, X. Lu, G. S. Kassab, and B. J. Tromberg, "Imaging coronary artery microstructure using second-harmonic and two-photon fluorescence microscopy," *Biophys. J.* **87**(4), 2778–2786 (2004).
4. M. B. Lilledahl, O. A. Haugen, C. D. L. Davis, and L. O. Svaasand, "Characterization of vulnerable plaques by multiphoton microscopy," *J. Biomed. Opt.* **12**(4), 044005 (2007).
5. T. T. Le, I. M. Langohr, M. J. Locker, M. Sturek, and J. X. Cheng, "Label-free molecular imaging of atherosclerotic lesions using multimodal nonlinear optical microscopy," *J. Biomed. Opt.* **12**(5), 054007 (2007).
6. H. W. Wang, T. T. Le, and J. X. Cheng, "Label-free imaging of arterial cells and extracellular matrix using a multimodal CARS microscope," *Opt. Commun.* **281**, 1813–1822 (2008).
7. H. W. Wang, I. M. Langohr, M. Sturek, and J. X. Cheng, "Imaging and quantitative analysis of atherosclerotic lesions by CARS-based multimodal nonlinear optical microscopy," *Arterioscler., Thromb., Vasc. Biol.* **29**, 1342–1348 (2009).
8. A. F. Pegoraro, A. Ridsdale, D. J. Moffatt, Y. Jia, J. P. Pezacki, and A. Stolow, "Optimally chirped multimodal CARS microscopy based on a single Ti:sapphire oscillator," *Opt. Express* **17**(4), 2984–2996 (2009).
9. S. Murugkar, C. Brideau, A. Ridsdale, M. Naji, P. K. Stys, and H. Anis, "Coherent anti-Stokes Raman scattering microscopy using photonic crystal fiber with two closely lying zero dispersion wavelengths," *Opt. Express* **15**(21), 14028–14037 (2007).
10. T. A. Pologruto, B. L. Sabatini, and K. Svoboda, "ScanImage: flexible software for operating laser scanning microscopes," *Biomed. Eng. Online* **2**, 13 (2003).
11. M. Shiomi, T. Ito, S. Yamada, S. Kawashima, and J. Fan, "Development of an animal model for spontaneous myocardial infarction (WHHLMI rabbit)," *Arterioscler., Thromb., Vasc. Biol.* **23**, 1239 (2003).
12. T. Itp, S. Yamada, and M. Shiomi, "Progression of coronary atherosclerosis relates to the onset myocardial infarction in an animal model of spontaneous myocardial infarction (WHHLMI rabbits)," *Exp. Anim.* **53**, 339–346 (2004).

Neurourology and Urodynamics 29:1350–1354 (2010)

The Effects of Chronic Hyperlipidemia on Bladder Function in Myocardial Infarction-Prone Watanabe Heritable Hyperlipidemic (WHHLMI) Rabbits

Masaki Yoshida,[1]* Koichi Masunaga,[2] Takashi Nagata,[3] Yo Satoji and,[4] Masashi Shiomi[5]
[1]Department of Urology, Kumamoto Hospital of Japan Labor Health and Welfare Organization, Kumamoto, Japan
[2]Department of Urology, Tokyo Metropolitan Geriatric Hospital, Tokyo, Japan
[3]Department of Urology, Toshiba Hospital, Tokyo, Japan
[4]Department of Urology, Graduate School of Medical Sciences, Kumamoto University, Kumamoto, Japan
[5]Institute for Experimental Animals, Kobe University School of Medicine, Kobe, Japan

Aims: Lower urinary tract symptoms (LUTS) are common in the aging population. LUTS cause profoundly negative impacts on their quality of life. Pathophysiology of LUTS is multifactorial, and recently, bladder ischemia and metabolic syndrome have been suggested as etiological factors. To evaluate chronic hyperlipidemia on bladder function, we examined the functional and histological changes of the bladder in myocardial infarction-prone Watanabe Heritable Hyperlipidemic (WHHLMI) rabbits. **Methods:** 20- to 24-month-old WHHLMI rabbits and age- and sex-matched control rabbits were prepared. Bladder functions were evaluated using cystometrograms and functional experiments with isolated bladder specimens. Histological studies of bladder and internal iliac arteries were performed with hematoxylin and eosin staining. The bladder was also stained immunohistochemically with mouse monoclonal S-100 antibodies and sheep polyclonal calcitonin gene-related peptide (CGRP) antibodies. **Results:** In cystometric examination, WHHLMI rabbits showed significantly shorter micturition interval, smaller voided volume with non-voiding contractions, and lower micturition pressure, as compared to control. The functional experiments showed that carbachol- and electrical field stimulation-induced contractions were significantly decreased in WHHLMI rabbits than those in control. In WHHLMI rabbits, cross-sections of internal iliac arteries showed significant atherosclerosis and thickening of media. Bladder showed thinner urothelium and decreased smooth muscle area in WHHLMI rabbits, as compared to control. WHHLMI rabbits showed a significant decrease in S-100 protein positive neurons, and an increased number of CGRP positive neurons. **Conclusions:** This study demonstrated that WHHLMI rabbits showed detrusor overactivity with decreased detrusor contraction. It is suggested that chronic hyperlipidemia contributes to the bladder dysfunction. *Neurourol. Urodynam. 29:1350–1354, 2010.* © 2010 Wiley-Liss, Inc.

Key words: LUTS; hyperlipidemia; ischemia; WHHLMI rabbits

INTRODUCTION

Lower urinary tract symptoms (LUTS) are common symptoms in the aging population.[1,2] Many people receive profoundly negative impacts on their quality of life from LUTS. The pathophysiology of LUTS is multifactorial, and various etiological factors have been suggested. Recently, metabolic syndrome and bladder ischemia have been suggested as important etiological factors.[3,4] Hyperlipidemia is a well-known risk factor for development and progression for cardiovascular and metabolic diseases. However, association between LUTS and hyperlipidemia is less clear.

Several studies have suggested the changes in bladder function using high cholesterol fed animal with ligation or balloon injury of bladder arteries.[5–7] The reports demonstrated that moderate bladder ischemia caused detrusor overactivity and increase contractile response to carbachol and EFS with moderate fibrosis in the bladder wall, whereas the severe bladder ischemia caused very weak bladder contraction and decreased response to the stimulation.[6] In the experimental model, acute development of atherosclerosis and acute bladder ischemia were induced. Thus, it seems not to be appropriate model for the gradual development of atherosclerosis and ischemia, as it develops in human. Watanabe heritable hyperlipidemic (WHHL) rabbit has been developed as an animal model for human familial hypercholesterolemia and atherosclerosis at first,[8] and now a myocardial infarction-prone Watanabe Heritable Hyperlipidemic (WHHLMI) rabbit as its new strain has been widely used as a model of hyperlipidemia, various organ ischemia, and related diseases.[9–11] Therefore, WHHLMI rabbits might be suitable for evaluation of bladder dysfunction due to chronic hyperlipidemia and slowly progression of atherosclerosis.

In the present study, we examined the functional and histological changes of bladder of WHHLMI rabbits and evaluated the effects of chronic hyperlipidemia and slowly progression of atherosclerosis with bladder ischemia on bladder function.

Conflict of Interest: Yoshida-Consultant: Astellas Pharm., Kissei Pharm., Pfizer. Speaker Honorarium: Astellas Pharm., Kissei Pharm., Pfizer.
Lori Birder led the review process.
*Correspondence to: Masaki Yoshida, MD, Department of Urology, Kumamoto Hospital of Japan Labor Health and Welfare Organization, 3-30-34-1402, Suizenji, Kumamoto 862-0950, Japan. E-mail: akko-maki@umin.net
Received 16 August 2009; Accepted 12 October 2009
Published online 1 February 2010 in
wileyonlinelibrary.com
DOI 10.1002/nau.20843

MATERIALS AND METHODS

Animals

This study was performed according to the Institutional Animal Care and Use in the Ethics Committee of Kumamoto University.

We prepared 20- to 24-month-old WHHLMI rabbits (n = 6), and age- and sex-matched Japanese white rabbits (n = 10) as controls. All WHHLMI rabbits were bred at and donated from the Institute of Experimental Animals of Kobe University School of Medicine. All rabbits were housed individually in metabolic cages in a room temperature and were fed standard rabbit chow (CR-3, Clea, Tokyo, Japan) and water ad libitum for 1 week. For evaluation of blood parameters, blood samples were taken from marginal ear vein after overnight fasting, and were referred to a commercial laboratory (SRL, Tokyo, Japan).

Evaluation of Bladder Function

The urine of each rabbit was automatically captured in a container under the cage, which was connected to an electronic pressure transducer (NA-021, Neuroscience, Tokyo, Japan). The frequency-volume chart (FVC) was recorded and monitored using an electronic pen recorder for 3 days. Then, the bladder was surgically exposed under anesthesia with sodium pentobarbital (35–50 mg/kg) and a catheter (OP-30-05, Eicom, Kyoto, Japan) was inserted into the bladder for cystometric examination, using constant infusion (1.0 ml/min) of saline into the bladder to elicit voiding. The catheter was connected to pressure transducer (TP-400T, Nihon-Kohden, Tokyo, Japan) for measurement of bladder pressure. Saline voided from urethral meatus was collected and measured to determine the voided volume, and the residual volume was measured by aspiration of the residual saline through the intravesical catheter, after the infusion was stopped at the beginning of a voided contraction. In our recording system, we determined bladder contractions over 4 cmH_2O as non-voiding contractions.

Functional Experiments

Under pentobarbital anesthesia, rabbits were sacrificed. Then, bladder was excised, and immersed in Krebs–Henseleit solution. Serosal layer was dissected and bladder strips were cut (approximately 2 mm wide and 8 mm long) from the dome of the bladder. The set up of the bladder specimen was performed as previously described.[12] The bladder strip was suspended in a 20-ml organ bath filled with Krebs–Henseleit solution. Then each preparation was connected to a force displacement transducer (TB-611T; Nihon-Kohden) and an isometric force was recorded and monitored on an ink-writing recorder. Concentration–response curves for carbachol were obtained by increasing the concentration in a stepwise manner after the response to the previous concentration had reached a plateau.

Contractile responses to 80 mM KCl were obtained by equimolar replacement of NaCl by KCl in Krebs–Henseleit solution. Electrical field stimulation (EFS) was generated between two parallel platinum wire electrodes (10 mm wide and 8 mm apart). Electrical impulses for field stimulation of the intramural nervous system of the strips were delivered with a stimulator (SEN-3301; Nihon-Kohden) and boosted by an amplifier (SEG-3104; Nihon-Kohden). The intrinsic nerves were stimulated with rectangular pulses of 0.3 msec duration and 40 V, at stimulation frequencies of 2–40 Hz. Trains of pulses lasted for 2 sec and there was an interval of 2 min between stimulations.

Histological Study

For the histological examination, bladders were fixed by immediate immersion in 0.2 M phosphate-buffered 4% paraformaldehyde (pH 7.4) at 4°C for 4–6 hr. After fixation, they were rinsed and cryoprotected with 10% sucrose in 0.01 M PBS at 4°C for 4 hr to overnight. The fixed specimens were dehydrated in graded ethanol and embedded in paraffin wax. Sections (5 μm) were cut, mounted onto precoated slides, and stained with hematoxylin and eosin (H&E) using standard methods.

To examine pathological changes of bladder vessels, distal portion of internal iliac arteries of two rabbits of both groups were also excised, sectioned transversely, and fixed and mounted onto slides. The prepared slides were stained with H&E.

Formaldehyde-fixed (4%) specimens of bladder in both WHHL (n = 6) and control (n = 10) rabbits were immunohistochemically stained for mouse monoclonal S-100 antibodies (Abcam, Cambridge, UK) and sheep polyclonal calcitonin gene-related peptide (CGRP) antibodies (Biogenesis, England, UK), as previously described.[13,14] During the staining procedure, the sections were pretreated with 3% H_2O_2 for 15 min to remove endogenous peroxidase activity from the tissue and immersed in a solution consisting of 1% bovine serum albumin, 5% NaCl, 1% gelatin, 0.15% glycine, and 1% Tween-20/100 ml of 20 mM Tris–HCl for 5 min to block non-specific background. The treated sections were exposed to the mouse monoclonal antibody S-100 or the sheep polyclonal antibody CGRP at 4°C for overnight. They were then exposed to the goat polyclonal antibody as a secondary antibody for primary antibody (DAKO, Copenhagen, Denmark) for 30 min. The reaction site was stained with diaminobenzidine and counter-stained with hematoxylin for 1 min. The sections were dehydrated through graded alcohols, cleared in xylene, and mounted.

All histological sections were examined using a microscope. A quantitative evaluation of the nerve density in the muscular and stromal layers was calculated, as previously described.[15] In brief, all separate nerve fibers and the constituting nerve fibers in each nerve bundle were counted. In this way, the total number of nerve fibers was obtained. After counting five fields, the mean nerve density score (MNDS) can be calculated.

Statistical Analysis

Values were expressed as mean ± SEM. Statistic analyses for comparisons between groups and between contraction curves were carried out using analysis of variance (ANOVA) and the Fisher's test. $P < 0.05$ was considered as a statistical significance.

RESULTS

There were no significant differences between WHHLMI and control rabbits in body weight, bladder weight, and blood serum examinations except total cholesterol and triglyceride level. Total cholesterol level (496 ± 58 mg/dl, n = 6) and triglyceride level (220.5 ± 22.5 mg/dl, n = 6) in WHHLMI rabbits were significantly higher, as compared to the control (19.5 ± 2.5 and 44.3 ± 4.4 mg/dl, respectively, n = 10). Examination of distribution of cholesterol revealed that WHHLMI rabbits showed three times higher amount of LDL fraction

than that of the control group (60.4 ± 2.8%, n = 6 and 19.2 ± 3.8%, n = 10, respectively).

In FCV, the number of micturition of WHHLMI rabbits (5.9 ± 0.9 times/day, n = 6) was significantly higher than that of the control (2.4 ± 0.6 times/day, n = 10), although the daily urinary volume (WHHLMI rabbits: 75.8 ± 9.3 ml, n = 6; control rabbits: 72.6 ± 10.4 ml, n = 10) was not different between groups. The micturition volume of the WHHLMI rabbits (16.0 ± 5.1 ml, n = 6) was significantly lower than that of the control (43.6 ± 6.9 ml, n = 10).

Typical recordings of the cystometric study in both groups are shown in Figure 1. The micturition volume was significantly lower, and micturition interval was significantly shorter in WHHLMI rabbits. WHHLMI rabbits also showed significantly lower micturition pressure. The post-voided residual urine did not show any significant differences in both groups (Table I).

In the functional study using bladder smooth muscle strips, 80 mM KCl-induced contractions of the control and WHHLMI rabbits (40.2 ± 8.0 mN, n = 10 and 37.6 ± 3.9 mN, n = 6, respectively) were not significantly different. As for carbachol- and EFS-induced contractions, the contractile response was showed as % of KCl-induced contraction. The concentration– and frequency–response curves for smooth muscle strips of WHHLMI rabbits showed substantially weaker contraction to the control (Fig. 2).

In the histological studies, the urothelium of WHHLMI rabbits was thinner than that of the control. Moreover, the amount of muscle fibers decreased and connective tissues increased in the WHHLMI rabbits. In WHHLMI rabbits, the cross-sections of distal portion of internal iliac arteries showed significant atherosclerosis lesions and thickening of media (Fig. 3).

Positive staining for the monoclonal antibody S-100 or the polyclonal antibody CGRP was indicated by red-brown color fibers in bladder of both groups. S-100 positive neurons were mainly detected in smooth muscles layer, and CGRP positive neurons were mainly detected in suburothelium (Fig. 4). WHHLMI rabbits showed significantly lower MNDS of S-100 positive neurons (14.5 ± 3.07, n = 6) and significantly higher MNDS of CGRP positive neurons (30.60 ± 5.43, n = 6), as compared to the control rabbits (29.50 ± 5.22 and 14.9 ± 3.00, n = 10, respectively).

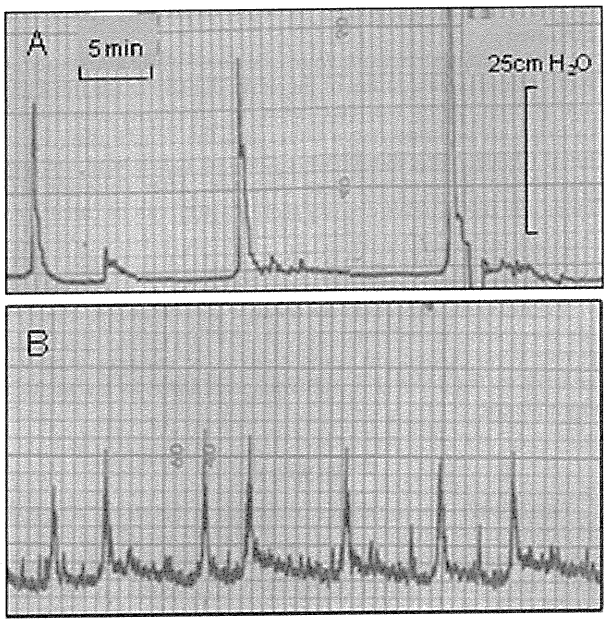

Fig. 1. Typical recordings of cystometrogram. **A**: Control rabbits; **B**: WHHLMI rabbits. WHHLMI rabbits showed shorter interval of micturition and lower micturition pressure, as compared to the control rabbits. There were non-voiding contractions in WHHLMI rabbits.

TABLE I. Comparison of Cystometic Findings Between the WHHLMI rabbits and the Control Group

	WHHLMI (n = 6)	Control (n = 10)
Micturition volume (ml)	6.82 ± 0.87*	20.8 ± 3.2
Interval of micturition (min)	4.52 ± 1.04*	13.87 ± 2.51
Micturition pressure (cmH_2O)	21.8 ± 2.1*	26.8 ± 2.3
Post void residual urine (ml)	1.20 ± 0.41	0.82 ± 0.23

Each value represents mean ± SEM. * $P < 0.05$; significantly different from the comparable value for control.
The bladder was surgically exposed under anesthesia with sodium pentobarbital, and a catheter was inserted into the bladder for cystometric examination, using constant infusion (1.0 ml/min) of saline into the bladder to elicit voiding. The catheter was connected to pressure transducer for measurement of bladder pressure. Saline voided from urethral meatus was collected and measured to determine the voided volume, and the residual volume was measured by aspiration of the residual saline through the intravesical catheter.

DISCUSSION

WHHLMI rabbits were developed as an animal model for myocardial infarction.[9,10] WHHLMI rabbits showed significant atherosclerotic lesions, and aortic atherosclerosis is observed grossly from 4-month old despite being fed normal chow, and the severity of atherosclerotic lesions increased significantly with aging.[9] WHHLMI rabbits are considered to be a good model for research on hyperlipidemia and atherosclerosis, and related ischemic diseases. Additionally, it has been reported that the lipid metabolism and the morphology of the atherosclerotic lesions of WHHLMI rabbits resemble those of humans.[9] Therefore, we used this model in the present experiment. The data of blood biochemistry in this study were consistent with the previous reports.[9–11]

It has been reported that 96% of the WHHLMI rabbits had cerebrovascular atherosclerosis. However, no rabbits showed involvement of penetrating arteries, and stenoses caused by cerebral atherosclerosis generally were milder than those associated with coronary or aortic atherosclerosis. Moreover, no behavioral or morphologic evidence of brain infarction were observed.[11] Hence, it is suggested that bladder dysfunction of WHHLMI rabbits observed in the present study may not be caused by apparent brain disorders. In the present study, we could not evaluate when bladder dysfunction started in WHHLMI rabbits. Evaluation for age-dependent changes of bladder function in WHHLMI rabbits will be needed to clarify it.

In FVC and cystometrogram, WHHLMI rabbits showed frequent voiding and detrusor overactivity (non-voiding contractions). However, micturition pressure of WHHLMI rabbits was significantly lower than that of control. In addition, the functional study with smooth muscle strips from WHHLMI rabbits showed the significantly decreased responses to carbachol and EFS, as compared to control. WHHLMI rabbits showed significant atherosclerosis lesions and thickening of media in the iliac arteries, suggesting slowly progression of ischemia of the bladder. Therefore, in WHHLMI rabbits, the chronic hyperlipidemia and/or atherosclerosis-